

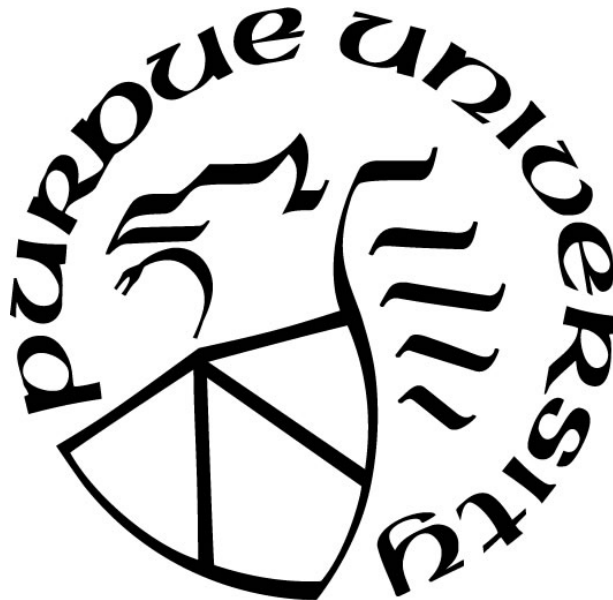
**INVESTIGATION OF ENERGETIC MATERIALS AND PLASMONIC
NANOSTRUCTURES USING ADVANCED ELECTRON MICROSCOPY
TECHNIQUES**

by
Xiaohui Xu

A Thesis

*Submitted to the Faculty of Purdue University
In Partial Fulfillment of the Requirements for the degree of*

Master of Science



School of Materials Engineering
West Lafayette, Indiana
December 2018

**THE PURDUE UNIVERSITY GRADUATE SCHOOL
STATEMENT OF COMMITTEE APPROVAL**

Dr. Lia Stanciu, Co-chair

School of Materials Engineering

Dr. Volkan Ortalan, Co-chair

School of Materials Engineering

Dr. Peilin Liao

School of Materials Engineering

Approved by:

Dr. David Bahr

Head of the Graduate Program

ACKNOWLEDGMENTS

Foremost, I would like to express my sincere gratitude to my advisor Dr. Volkan Ortalan for his great support in the past two years. His enthusiasm, motivation and profound knowledge in electron microscopy have guided me and significantly influenced me academically. I really appreciate his wise suggestions and help whenever I had problems in my experiments or research. Next, I also want to thank my group members, Subhajit Kundu, Tugba Isik and Garrett Mitchell. They have given me kind help for my research work and I learned a lot by talking with them, especially Subhajit. Finally, I would like to thank both my parents and my boyfriend for always supporting me and encouraging me to become better.

TABLE OF CONTENTS

LIST OF TABLES	5
LIST OF FIGURES	6
ABSTRACT	8
CHAPTER 1. INTRODUCTION	9
CHAPTER 2. BACKGROUND	12
2.1 Theory of laser-matter interaction	12
2.2 Principles of ultrafast transmission electron microscope (UTEM).....	14
2.3 Energetic materials.....	15
2.4 Basics of plasmonics.....	18
CHAPTER 3. ELECTRON MICROSCOPY STUDY ON ENERGETIC MATERIALS.....	21
3.1 DP simulation of HMX, RDX and CL-20	21
3.1.1 HMX	22
3.1.2 RDX.....	24
3.1.3 CL-20.....	26
3.2 Investigation of HMX using UTEM and tomography	28
CHAPTER 4. LASER-INDUCED WELDING OF PLASMONIC NANOSTRUCTURES.....	33
4.1 Laser-induced inter-welding and alloying of silver and gold nanoparticles.....	33
4.1.1 Experimental methods	33
4.1.2 Results and discussion	34
4.2 Laser-induced welding of silver nanowires	39
4.3 Laser-induced merging of gold nanoparticles into silver nanowires	41
REFERENCES	44
VITA	52
PUBLICATIONS.....	53

LIST OF TABLES

Table 1. Laser types based on different criteria. ⁴²	12
Table 2. Some figures of the polymorphs of HMX. Reproduced from literature. ⁶⁵	16
Table 3. Structural information about RDX.	17
Table 4. Summary of the crystallographic data for five forms of CL-20.	18
Table 5. Simulated DPs of HMX phases using CrysTBOX.	22
Table 6. Simulated DPs of RDX phases using CrysTBOX.	24
Table 7. Simulated DPs of CL-20 phases using CrysTBOX.	26

LIST OF FIGURES

Figure 1. (a) A schematic of laser-matter interactions based on different time scales. (b) Heat-affected zones caused by three lasers with different pulse widths. ⁴⁸	13
Figure 2. Schematic of ultrafast transmission electron microscope (UTEM). ⁴⁹	14
Figure 3. Molecular structures of HMX, RDX and CL-20 respectively.	15
Figure 4. (a) A schematic showing the excitation of SP and SPP in a bulk metallic material. ⁸¹ (b) LSP induced inside a single nanoparticle directly by a light wave. ⁸²	19
Figure 5. The concept of Yee Lattice. ⁸⁷	20
Figure 6. A window from CrysTBOX CellViewer, showing both the simulated diffraction pattern (left) under a specific zone axis and the atomic lattice of the material (right).	21
Figure 7. Bright field TEM images of HMX samples with different morphologies: (a) flower-like structures, (b) flakes and (c) strips.	29
Figure 8. Bright field TEM images showing (a) a slightly degraded and (b) a seriously degraded HMX sample. The number and size of bubbles are increased with electron beam exposure.	29
Figure 9. Selected area diffraction pattern of HMX from two different locations (a, c) and corresponding simulated patterns (b, d) respectively by CrysTBOX.	31
Figure 10. (a) Bright field TEM image of a strip-shaped HMX piece. (b, c) 3D reconstruction of the same region viewed from different directions.	32
Figure 11. Bright field TEM images of a NP dimer before laser exposure (a) and after being exposed to pulsed laser for 2s (b), 10s (c), 20s (d), 100s (e) and 1000s (f). A duty cycle mode was used with 10 laser pulses on and 90 pulses off in each cycle. Laser power was 0.4mW.	35
Figure 12. HAADF-STEM images of Ag-Au NP dimers and corresponding EDX mapping.	36
Figure 13. HAADF-STEM images and EDX mapping showing Ag wrapping up Au NPs when (a) Ag NP is larger than Au NP and (b) Ag NP is smaller than Au NP. In (c), the Ag NP in the red square wraps up two Au NPs.	37

- Figure 14. (a) Absorption efficiencies of four types of dimers: 1. Ag NP (60nm) + Ag NP (50nm), 2. Au NP (60nm) + Au NP (50nm), 3. Ag NP (60nm) + Au NP (50nm), 4. Ag NP (60nm) + Au@Ag core-shell NP with a core size of 46nm and shell thickness of 2nm. (b) Comparison of the absorption efficiencies of Ag-Au NP dimers with different Ag NP sizes but the same Au NP size. Curve 1: Ag NP (50nm) + Au NP (50nm) with a 4nm overlapping; curve 2: Ag NP (60nm) + Au NP (50nm) with a 4nm overlapping. 39
- Figure 15. Bright field TEM images of a silver nanowire junction after different number of laser pulses. 40
- Figure 16. Bright field TEM images of two Ag NW junctions after laser irradiation and diffraction patterns from different regions (shown by the arrows) of the NWs. 41
- Figure 17. Real-time visualization of the merging of Au NPs into the Ag NW. 42
- Figure 18. HAADF-STEM images and EDS maps of Ag and Au showing different stages of the merging process as described in the text. 43

ABSTRACT

Author: Xu, Xiaohui. MS

Institution: Purdue University

Degree Received: December 2018

Title: Investigation of Energetic Materials and Plasmonic Nanostructures Using Advanced Electron Microscopy Techniques

Committee Chair: Lia Stanciu and Volkan Ortolan

Investigation of laser-matter interaction has been an important research topic which is closely related to applications in various fields including industry, military, electronics, photonics, etc. With the advent of ultrafast transmission electron microscope (UTEM), in situ investigation of the interaction between pulsed laser and nanostructured materials becomes accessible, with unprecedented spatial and temporal resolution. Here, we studied two categories of materials with the help of UTEM, namely, energetic materials and plasmonic nanostructures. The results demonstrate that UTEM provides a novel and convenient way for the investigation the structural and morphological change of energetic materials under external stimuli at nanoscale. Also, UTEM makes it possible to visualize the light-induced welding between plasmonic nanostructures at real time, which helps to reveal more details about the mechanisms involved. Furthermore, we studied the formation of some novel structures by combing different gold and silver nanostructure.

CHAPTER 1. INTRODUCTION

Laser, as a special kind of light, owns some unparalleled advantages including high spatial and temporal coherence, high intensity and excellent directionality. After laser was first built in 1960, its application in various fields was continuously explored, and it has been widely used in medicine, industry, military, etc.¹⁻⁵ In the field of materials science, laser has been receiving more and more attention due to its capability of modifying materials and microstructures locally. For example, laser heating of materials is extensively used for materials treatment such as welding, drilling, cutting, alloying, surface hardening, heat treatment, etc. Furthermore, the possibility of using laser as a versatile tool for fabricating and sculpting nanostructures has prompted the recent interest in multiple material systems. In 2016, M. Terakawa et al reported the fabrication of three-dimensional (3D) metal microstructure by laser-induced photoreduction.⁶ R. Jin et al successfully grew anisotropic Ag nanoparticles through laser-induced plasmon excitation.⁷ Besides, the joining of nanoparticles by laser has been proved to be ideal for the assembly of some complex functional materials.^{8,9}

The research on laser-matter interaction has provided essential theory for the exploitation of laser applications. Laser-matter interaction is an interdisciplinary and complex subject.¹⁰ To give readers a better understanding, the theory of laser-matter interaction is given in the Background section. Despite the progress in the study of laser-matter interactions, *in situ* study is very scarce due to the difficulty in conducting laser experiments inside electron microscope system. This has prevented us from gaining a better understanding towards laser-induced welding of nanostructures since a complete picture of the structural and compositional evolution is missing. Fortunately, the advent and development of ultrafast transmission electron microscope (UTEM) makes *in situ* investigation of laser-induced dynamical processes possible, with unprecedented spatial and temporal resolution.¹¹⁻¹³ The concept of UTEM (previously was called high-speed electron microscopy) was first proposed by Bostanjoglo in 2002.¹⁴ Later, the first femtosecond UTEM in stroboscopic mode was achieved by Zewail et al¹⁵ at Caltech, in order to realize the 4D visualization of complex structures nondestructively with the spatial resolution of transmission electron microscopy (TEM). The direct visualization enabled by UTEM helps to reveal more details about the structural evolution during welding as well as more clues of the mechanisms

involved. The structure and working principles of UTEM will be introduced in detail in the Background section.

Among various types of laser-matter interaction, two important categories are investigated in this work. One is laser-induced reactions of energetic materials, while the other is laser-induced welding of plasmonic nanomaterials. Energetic materials refer to materials with high amount of stored chemical energy that can be released under specific conditions. To get a better understanding of currently popular energetic materials (like RDX, HMX, CL-20) and improve their performance, it is critical to learn more about their microstructures and properties. UTEM provides to be an ideal tool for this purpose. On one hand, as an electron microscope, UTEM is capable of characterizing the crystal structures and morphologies of energetic materials. On the other hand, we can examine the chemical stability of different energetic materials as well as thermal reactions initiated by laser between them. In a word, UTEM provides a way to study energetic materials at nanoscale with decent spatial and temporal resolution, thus giving information about energetic materials that cannot be obtained by other experimental approaches. Laser-induced welding is an important topic in the field of materials science and engineering. Specifically, the welding of noble metallic materials, including gold and silver, has been extensively studied due to the wide applications of gold and silver in the field of electronics, plasmonics, etc. For example, noble metallic nanowires (NWs) have emerged as critical components in nanoelectronics and photonics owing to their use as interconnects and/or circuit elements.¹⁶⁻²⁰ Welding noble metal nanowires together to obtain junctions with low resistances and high optical transparency has been largely exploited in the development of transparent conductors used in a wide variety of applications such as solar cells, touch screens and organic light emitting diodes.^{11,21} It has been demonstrated that welded Ag nanowire networks showed excellent promise in replacing the conventional transparent conductor indium tin oxide (ITO).²²⁻²⁴ Another example is the application of noble metallic nanoparticles (NPs) in the field of biosensing,²⁵ imaging,²⁶ cancer therapy,²⁷ nanophotonics,²⁸ etc. Those applications are closely related to the unique optical properties of metallic NPs originating from the collective oscillation of conduction electrons under an external electromagnetic radiation, known as localized surface plasmon resonance (LSPR). It has been found that the LSPR behavior of gold or silver NPs is strongly dependent on the morphology of nanoparticles, including their size, shape, composition, etc.²⁹⁻³¹ The optical or plasmonic properties of metallic NPs can also be modified by laser welding,

which has attracted much interest in recent years.^{9,32,33} Because of the ‘hot spot’ effect³⁴, NPs can be preferentially heated at the interparticle gap, resulting in a higher welding efficiency compared with the uniform hot-plate welding.

Two main questions are proposed out of the two categories discussed above. Firstly, for the study of energetic materials, despite the fruitful research on the combustion mechanisms and heat transfer process, very limited number of studies have thoroughly investigated the crystal structures as well as the microstructural change of energetic materials at real time experimentally. It might be possible to simulate the structural evolution of energetic materials under thermal excitation, but experimental observation is always necessary to examine the correctness of simulations. Secondly, for the study of laser-induced welding of plasmonic materials, although the welding of gold or silver nanostructures have been investigated in numerous studies, most of them are focused on the welding between the same structures with the same composition, such as Ag NW-Ag NW welding,¹⁷ Ag NP-Ag NP welding,³² Au NP-Au NP welding,³³ etc. Study on the welding between different noble metals or different nanostructures is relatively limited. However, based on the difference in optical, plasmonic and chemical properties of different noble metallic nanostructures, their inter-welding might provide a novel way to combine their features and get functional nano-bolcks with unique properties. It has been already demonstrated that intricate nanostructures composed of basic Ag and Au structures own unique optical properties. For example, Ag coated Au nano-dumbbells show interesting LSPR behavior which leads to significantly enhanced SERS activity,³⁵ and compositionally modulated bimetallic nanowires³⁶⁻³⁸ show great potential in future electronic devices as spin valves, optical labels, etc.³⁹⁻⁴¹ Therefore, we infer that laser welding of silver and gold nanostructures might result in intricate geometries with novel properties.

Based on questions above, two projects are established and completed in this work. The first one is an electron microscopy study of energetic materials using UTEM, and the second one is direct visualization of laser-induced welding of different plasmonic nanostructures. They are discussed in detail in Section 3 and 4. In conclusion, this work is aimed to argue that UTEM is an ideal technique to study such laser-induced dynamics with real-time visualization and unprecedented resolution, and laser-induced welding provides a valuable approach to synthesize novel plasmonic nanostructures.

CHAPTER 2. BACKGROUND

2.1 Theory of laser-matter interaction

A laser is a device emitting light through a process of optical amplification based on the stimulated emission of electromagnetic radiation. Lasers can be categorized as shown in Table 1.⁴² When the laser beam interacts with a material, the incident light can be reflected or absorbed or transmitted. The laser beam can interact with the matter to induced either a thermal, chemical process, or both⁴³ resulting in three possible mechanisms of laser-matter interaction, namely, photothermal, photochemical and photophysical.⁴⁴

Table 1. Laser types based on different criteria.⁴²

Criteria	Laser types
Lasng material	Gas laser (He-Ne, Ar, CO ₂ ...), chemical laser (HF, ² HF...), dye lasers, Metal-vapor laser (HeCd, HeHg, HeSe...), solid state laser (Ruby, Nd:YAG...), semiconductor laser (GaN, InGaN...)...
Wavelength	Ultraviolet (UV) laser (190-340 nm), blue laser (~480 nm), green laser (~540 nm), red laser (~630 nm) ...
Continuity	Continuous wave (CW) laser, pulsed laser
Pulse duration	Microsecond (10 ⁻⁶ s) laser, nanosecond (10 ⁻⁹ s) laser, picosecond (10 ⁻¹² s) laser, femtosecond second (10 ⁻¹⁵ s) laser...

Depending on the phonon spectrum, the incoming photons in the laser beam will first be absorbed and couple into available electronic states. After the absorption, the energy is transferred to the ions in the lattice through repeated emission of phonons. To describe this process more quantitatively, we will define important parameters here, including the electron cooling time τ_e , lattice heating time τ_i , and lase pulse duration τ_L . Normally the electron cooling time is much smaller than the lattice heating time ($\tau_e \ll \tau_i$).⁴⁵ τ_i is the time needed for the excited electronic states to transfer energy to phonons. For most metals, this time is on the order of 10⁻¹²-10⁻¹⁰s, while for non-metals, due to the variation in absorpion mechanisms, τ_i can be as long as 10⁻⁶s.⁴⁴ τ_i is crucially important as it determines the boundary between strictly photothermal and photochemical routes, and the boundary between “long” and “short” pulses. When the laser duration τ_L is rather long compared with τ_i , the energy in the electronic states has enough time to transfer into phonons

thus resulting in the temperature increase of the target material.⁴⁶ In other words, one can consider the absorbed laser energy as being directly transformed into heat ignoring the transient electronically excited states. This process is called a thermal or photothermal process, and the material response can be treated in a purely thermal way. For most metals, laser with a pulse duration longer than nanosecond usually induces photothermal processes. When the electron-phonon energy transfer time is very long compared with laser pulse duration, namely, $\tau_e \gg \tau_L$, the overall thermalization is very slow, and the temperature of the target material remains relatively unchanged during laser irradiation. Meanwhile, large excitations can be built up in the intermediate states, and the excitation energy can be sufficient to directly break bonds (photo-decomposition).⁴⁷ This type of non-thermal process is photochemical process. For laser pulse duration that satisfies $\tau_e \ll \tau_L \ll \tau_i$, both thermal and non-thermal process will take place, which is referred to as photophysical process.

Figure 1 shows different material responses to lasers with different pulse durations.⁴⁸ For CW lasers and relatively long pulsed lasers such as nanosecond laser, the materials are removed primarily by melting, which generates quite a significant heat-affected zone in the material; while for ultrashort pulsed lasers, such as femtosecond or picosecond laser, high-precision material processing can be achieved, as shown in Figure 1b.

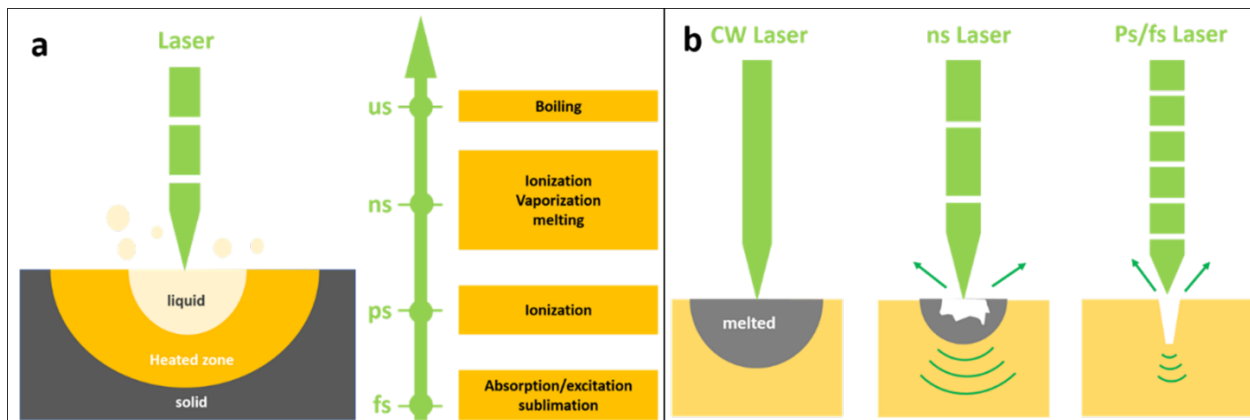


Figure 1. (a) A schematic of laser-matter interactions based on different time scales. (b) Heat-affected zones caused by three lasers with different pulse widths.⁴⁸

2.2 Principles of ultrafast transmission electron microscope (UTEM)

Figure 2 illustrates the design of an UTEM.⁴⁹ Two laser beams are coupled with the microscope. The sample excitation laser (pump pulse) is used to initiate structural changes of the sample and set the starting point of the experiment. The second laser, called electron generating laser (probe pulse), is used to stimulate photoemission of electrons from a photocathode. This method is called “pump-probe scheme”.^{50–52} Based on the reversibility of the reactions or structural changes involved, UTEM can be operated in two different modes, namely, single-shot mode and stroboscopic mode. Single shot mode is used to record irreversible processes, such as crystallization^{53,54} and phase transition.^{55,56} After the sample is excited by a single pump pulse, the structural changes along with time are recorded continuously by single pulses of electrons generated from the photocathode, and each pulse contains sufficient electrons to form an image.⁵⁷

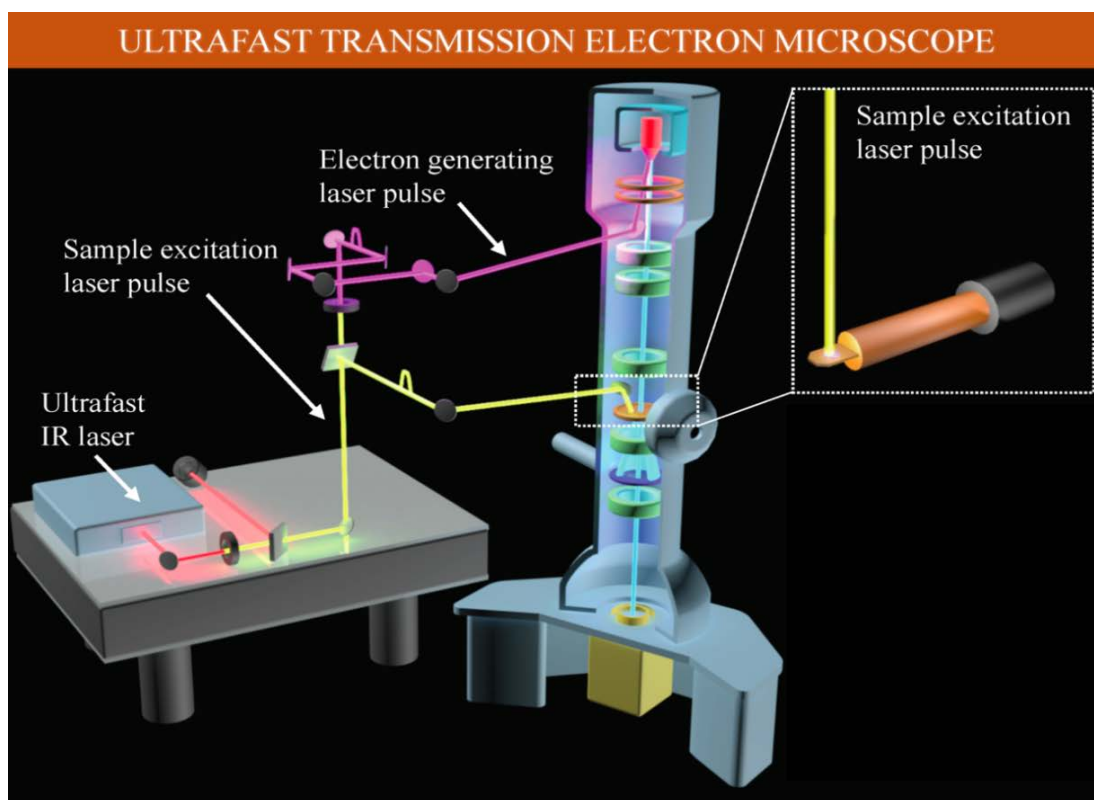


Figure 2. Schematic of ultrafast transmission electron microscope (UTEM).⁴⁹

The stroboscopic mode, or single-electron mode, is used to study reversible and transient dynamics such as metal-insulator structural dynamics,¹³ mechanical vibrations^{58–60} and

nanofriction.⁶¹ Under stroboscopic mode, the photocathode is illuminated with low energy laser pulses, so each pulse can be regarded as containing only one single electron packet. By setting the single-electron pulse at the same frequency and a specific time delay with respect to the pump pulse, a snapshot of the process at that particular time delay can be obtained through the summation of a train of coherent single-electron packets. Different time delays are set to gather information at different stages of the process, resulting in the four-dimensional (4D) microscopy study of structural changes. The most important advantage of stroboscopic mode is that the Coulomb repulsion between electrons is eliminated, thus eliminating the spreading of electrons in space and time. As a result, a higher spatiotemporal resolution is achieved.

In conclusion, UTEM has been proved to be an excellent tool to study nanoscale or atomic scale dynamic processes. Both single-electron mode and single-shot mode own unique advantages and, inevitably, inherent limitations. Selection of the operation mode will specifically depend on the dynamic process under investigation.

2.3 Energetic materials

Energetic materials are materials which can release a high amount of energy during detonation and/or deflagration. They have wide applications in military and commercial fields. Typical energetic materials include explosives, pyrotechnic compositions, propellants, fuels, etc.⁶² Among various energetic materials, HMX has been studied extensively in the past few decades as a nitroamine explosive. The full name of HMX is Octahydro-1,3,5,7-tetranitro-1,3,5,7-tetrazocine, and it is also known as cyclotetramethylene-tetranitramine or octogen.⁶³ The molecular structure of HMX is shown in Figure 3,⁶⁴ from which we can see that it is composed of an eight-membered ring of alternating carbon and nitrogen atoms with a nitro group attached to each nitrogen atom. Due to its high density and high molecular weight, HMX is regarded as one of the most powerful chemical explosives.

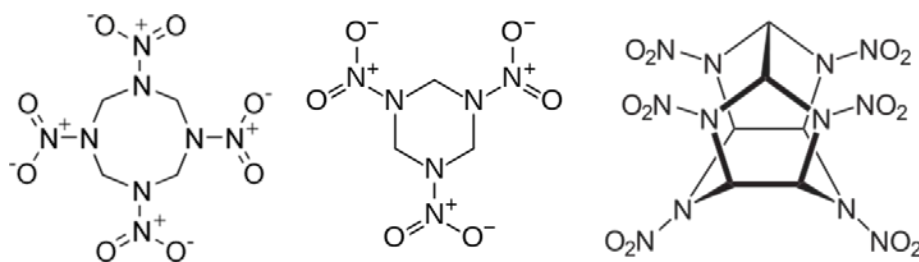


Figure 3. Molecular structures of HMX, RDX and CL-20 respectively.

HMX can exist in different crystal structures with different thermal stability, reactivity and sensitivity. Up to now, there are four known polymorphs of HMX, namely α , β , γ , and δ . Each of them exist within a specific stability range.⁶⁵ β -HMX has a monoclinic structure with P21/c symmetry and two molecules per unit cell. It is the most stable phase and is widely used in military. The α phase has an orthorhombic structure with Fdd2 symmetry and it is stable in the temperature range of 376–435K.⁶⁶ The hexagonal δ -HMX phase is stable from 455K to the melting point, while γ -HMX is metastable compared to the other HMX polymorphs.⁶⁶ The crystal structure and other features of four HMX polymorphs are summarized in Table 2.

Table 2. Some figures of the polymorphs of HMX. Reproduced from literature.⁶⁵

Polymorph	Density (mg.cm ⁻³)	Crystal system	Space group
β -HMX	1.903	monoclinic	P2 ₁ /c
α -HMX	1.87	orthorhombic	Fdd2
γ -HMX	1.82	monoclinic	Pc or P2/c
δ -HMX	1.78	hexagonal	P6 ₁ 22

Another chemical explosive that is closely related to HMX is RDX, whose full name is 1,3,5-trinitro-1,3,5-triazinane. The molecular structure of RDX is shown in Figure 3,⁶⁷ which have the same N-NO₂ bonds as HMX. RDX is a widely used energetic material for various propellants and explosive formulations in military applications because of its inexpensive synthesis compared with other explosives, high performance level and its relatively low sensitivity to external conditions. So far, five polymorphic phases of RDX is detected in the solid state, namely α , β , γ , δ and ϵ phase.⁶⁸⁻⁷¹ α -RDX is one stable form at ambient conditions and lower temperatures. Information about the space group and lattice parameters of four polymorphs of RDX is shown in Table 3 below. In addition to physical and chemical structures, size and size distribution of explosives also matters. Song and Li⁷² investigated the effect size distribution on mechanical sensitivity and thermal stability of RDX by preparing two set of samples. Results showed the direct relation between particle size and safety properties. Smaller particles showed less mechanical and thermal sensitivity, but it is also observed that sample with a broad size distribution is more sensitive to mechanical action than the narrow size distribution sample when the particle sizes are close.

Table 3. Structural information about RDX.

Polymorph	Density (mg.cm ⁻³)	Crystal system	Space group
α -RDX ⁷³	1.794	orthorhombic	Pbca
β -RDX ⁷⁴	1.795	orthorhombic	Pca21
γ -RDX ⁶⁸	2.267	orthorhombic	Pca21
ϵ -RDX ⁷¹	2.266	orthorhombic	Pca21

In the 1980s, a new type of nitroamine explosive was synthesized, known as HNIW or CL-20. It has the full name of 2,4,6,8,10,12-hexanitro-2,4,6,8,10,12-hexaazaisowurtzitane and a molecular structure shown in Figure 3.⁷⁵ Currently it's one of the most promising candidates for explosive and propellant formulations. The basic structure of CL-20 molecule is a rigid isowurtzitane cage that contains two five membered rings and one six membered ring. There are also six nitro groups on each bridging nitrogen atom along with the cage, which can facilitate the rapid release of high energy. Compared with conventional monocyclic explosives such as HMX and RDX, CL-20 owns low ratio of carbon atoms to nitramine moieties, high oxygen balance and increased density, all of which make CL-20 be the high-energy material of the next generation. Because of the spatial orientation of those nitro groups relative to the five- and six-membered rings, and the differences in crystal lattice packing (as well as number of molecules in one unit cell), five different polymorphs of CL-20 have been reported. Among them, ϵ -CL-20 has gained the most attention due to its high density compared with other polymorphs. Higher density means a higher rate of detonation and greater stability towards shock. It has been reported that the explosive performance of ϵ -CL-20 was found to be approximately 14% higher than that of HMX.⁷⁶ The crystallographic data for the five polymorphs of CL-20 is shown in Table 4, based on calculations of Nielsen et al.⁷⁷ It should be mentioned that for the α -CL-20 we are talking about is in fact in the hydrate form, since α -CL-20 is not stable without water filling in the lattice voids. The thermodynamic stability of four basic polymorphs under ambient condition has also been studied. Two different rankings of stability have been reported: one is $\epsilon > \gamma > \alpha > \beta$,⁷⁸ while another is α (hydrate) $> \epsilon > \alpha$ (anhydrous) $> \beta > \gamma$.⁷⁹ Despite of the difference in ranking, it's commonly accepted that ϵ phase is thermodynamically the most stable form of CL-20 with the highest density (if α -hydrate is not considered).

Table 4. Summary of the crystallographic data for five forms of CL-20.

Polymorph	Density (mg.cm ⁻³)	Crystal system	Space group
α-CL-20	1.981	orthorhombic	Pbca
β-CL-20	1.985	orthorhombic	Pca21
γ-CL-20	1.916	monoclinic	P21/c
ε-CL-20	2.044	monoclinic	P21/c
ζ-CL-20	2.275	monoclinic	P21/c

2.4 Basics of plasmonics

In recent years, plasmonics has attracted considerable attention due to their impact on the new fields of research. This new interest is linked with the rapid development of nanophotonics. The science of plasmonics deals with resonant interaction between electromagnetic radiation (light in particular) and free electrons at the interface between a metal and a dielectric material (e.g. air or glass), when exposed to an incident light. This interaction results in the collective oscillation of conduction electron gas. The quantum of this plasma oscillation is called plasmon, and the combination of the surface plasmon (SP) in the metal and the electromagnetic wave at the metal-dielectric interface is called surface plasmon polariton (SPP), as shown in Figure 4. SPPs are shorter wavelength than the incident light (photons), which means that they have narrower spatial confinement and higher local field intensity. Since the momentum of SPP wave is larger than that of light in free-space photon, there is a momentum mismatch between the light and SPP, which must be overcome by some coupler configurations such as prism couplers, grating couplers, etc.,⁸⁰ as shown in Figure 4a.⁸¹ However, for nanomaterials, there is a special kind of plasmon called localized surface plasmons (LSPs), which are nonpropagating excitations of free electrons of metallic structures. LSPs can be directly excited by light illumination, which means that nanostructures, such as nanoparticles and nanowires, can be used directly as plasmonic materials without any coupling, based on their response towards photons and electrons (Figure 4b)⁸². Therefore, the plasmonic study of nano-metallic materials, mainly noble metals (Au, Ag, etc.), has received much attention.

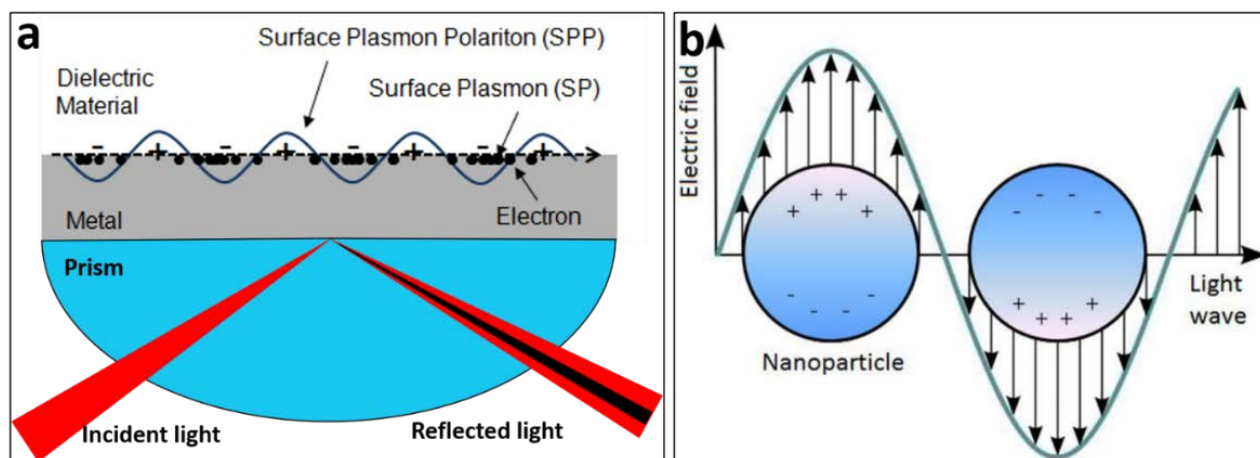


Figure 4. (a) A schematic showing the excitation of SP and SPP in a bulk metallic material.⁸¹ (b) LSP induced inside a single nanoparticle directly by a light wave.⁸²

The optical properties of plasmonic materials can be simulated by multiple methods. Some representative methods are finite-difference time-domain (FDTD) method,⁸³ finite element method (FEM),⁸⁴ boundary element method (BEM),⁸⁵ discrete dipole approximation (DDA),⁸⁶ etc. Specifically, FDTD method was used in this work to model the optical response of gold/silver nanostructures. FDTD method is featured by the idea of Yee Lattice or Yee Grid (Figure 5)⁸⁷. In 1966, Kane Yee proposed a method to spatially stagger the vector components of E-field and H field about rectangular unit cells of a Cartesian computational grid so that each E-field vector is located midway between a pair of H-field vectors, and vice versa.⁸³ In this way, the time-dependent Maxwell's equations are discretized using central-difference method to the time and space partial derivatives, and the resulting equations can be solved in a leapfrog manner. Different types of software have been developed for FDTD simulation, among which Meep is an open-source software package that was used in this work.⁸⁸

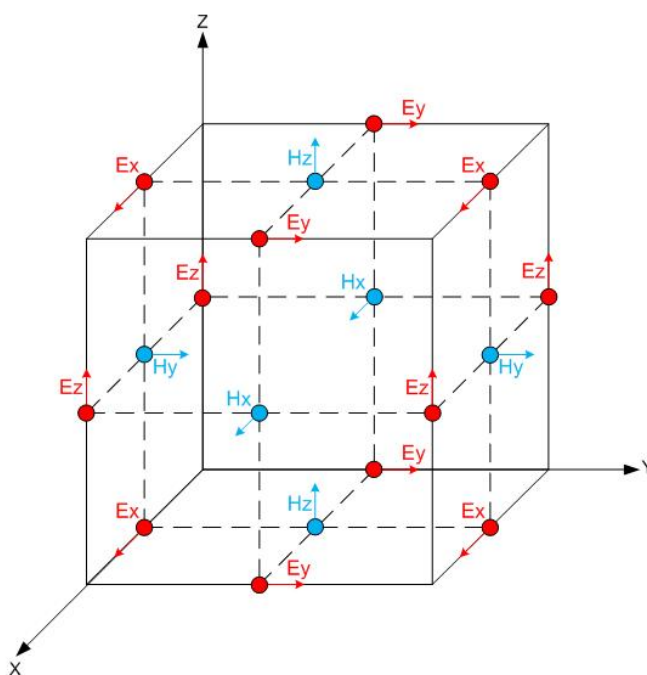


Figure 5. The concept of Yee Lattice.⁸⁷

3.1.1 HMX

Among four polymorphs of HMX introduced in the previous section, three of them have their detailed crystallographic data accessible currently, namely, α -HMX, β -HMX and γ -HMX. Their simulated DP patterns under some common zone axis are shown here:

Table 5. Simulated DPs of HMX phases using CrysTBOX.

Phase DP Zone axis	α -HMX	β -HMX	γ -HMX
100			
110			
111			
210			

Table 5. Continued.

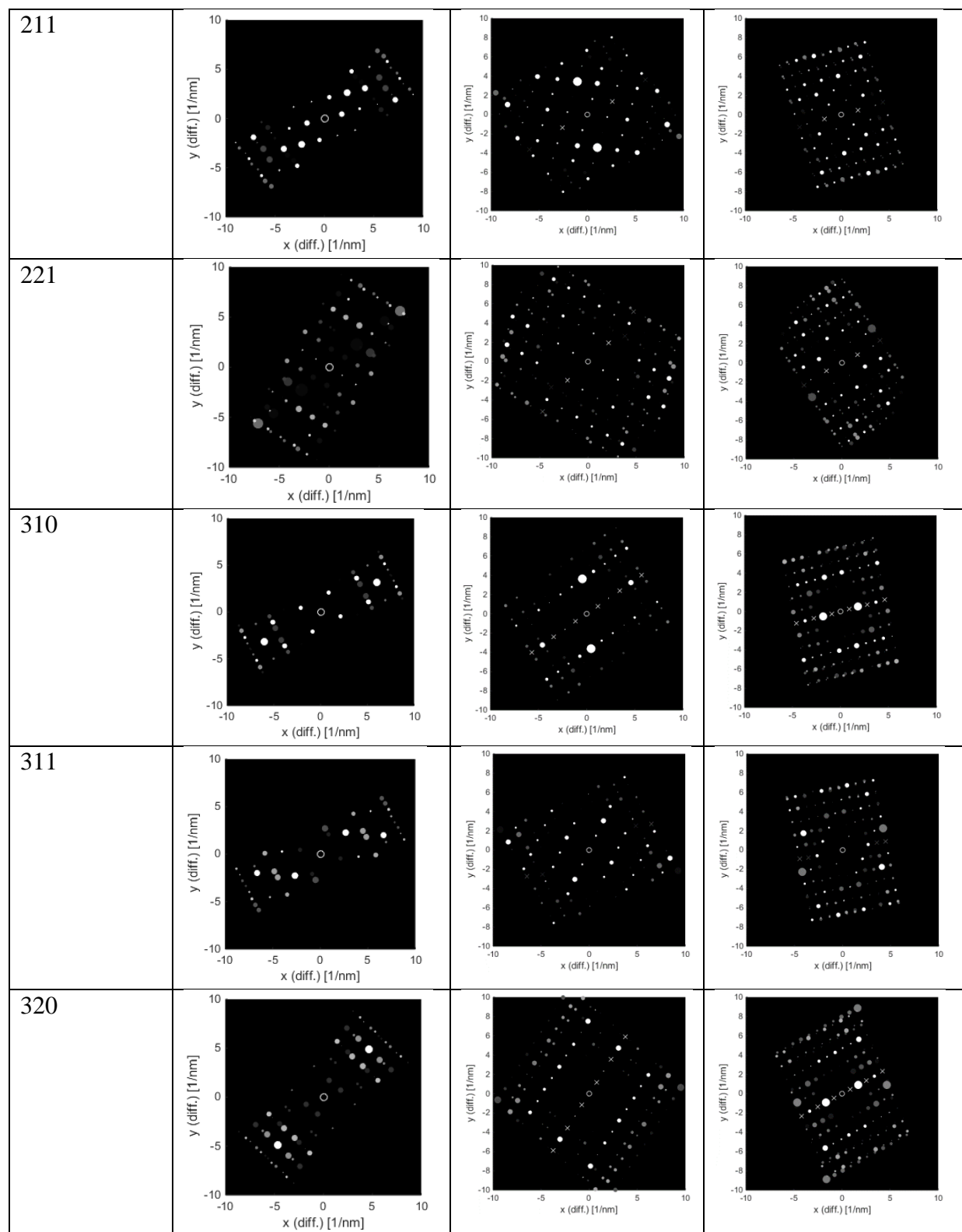
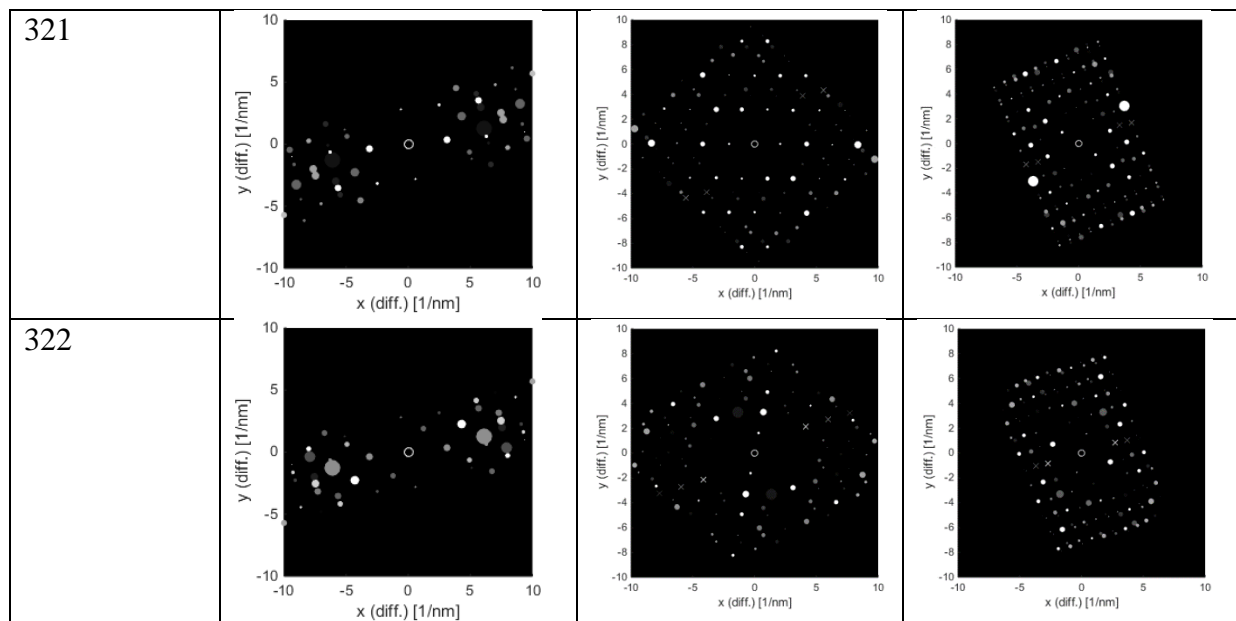


Table 5. Continued.



3.1.2 RDX

The diffraction pattern of four polymorphs of RDX is simulated and shown below:

Table 6. Simulated DPs of RDX phases using CrysTBOX.

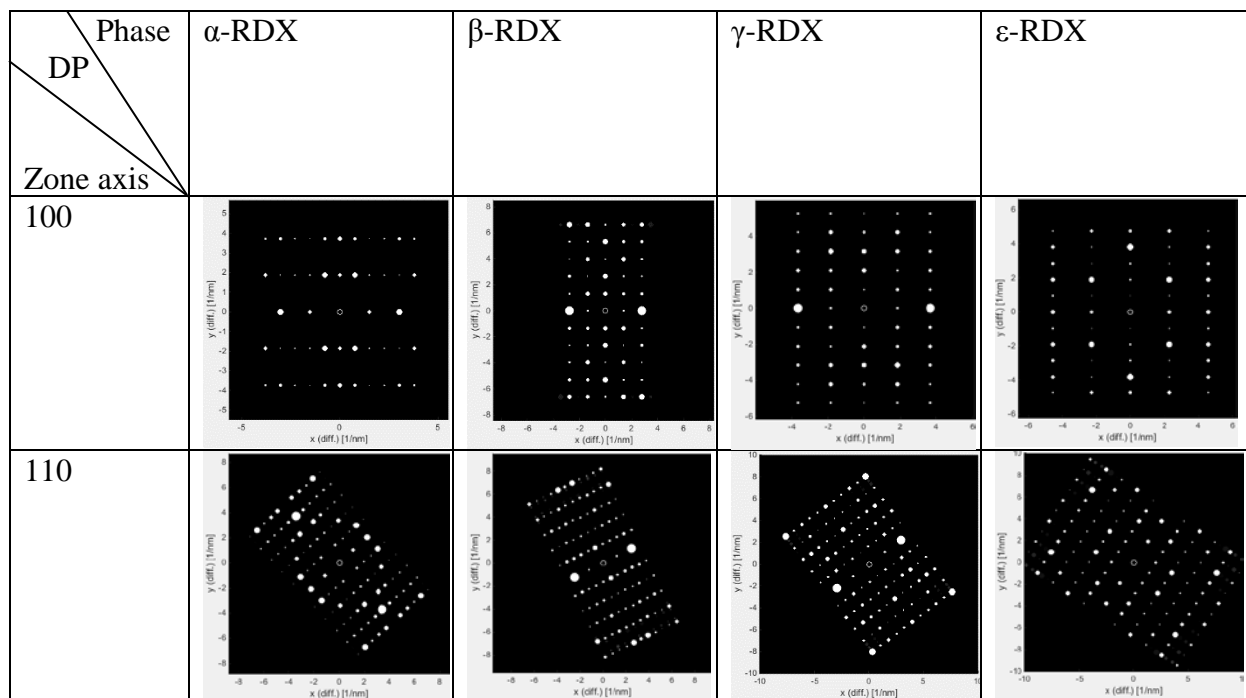


Table 6. Continued.

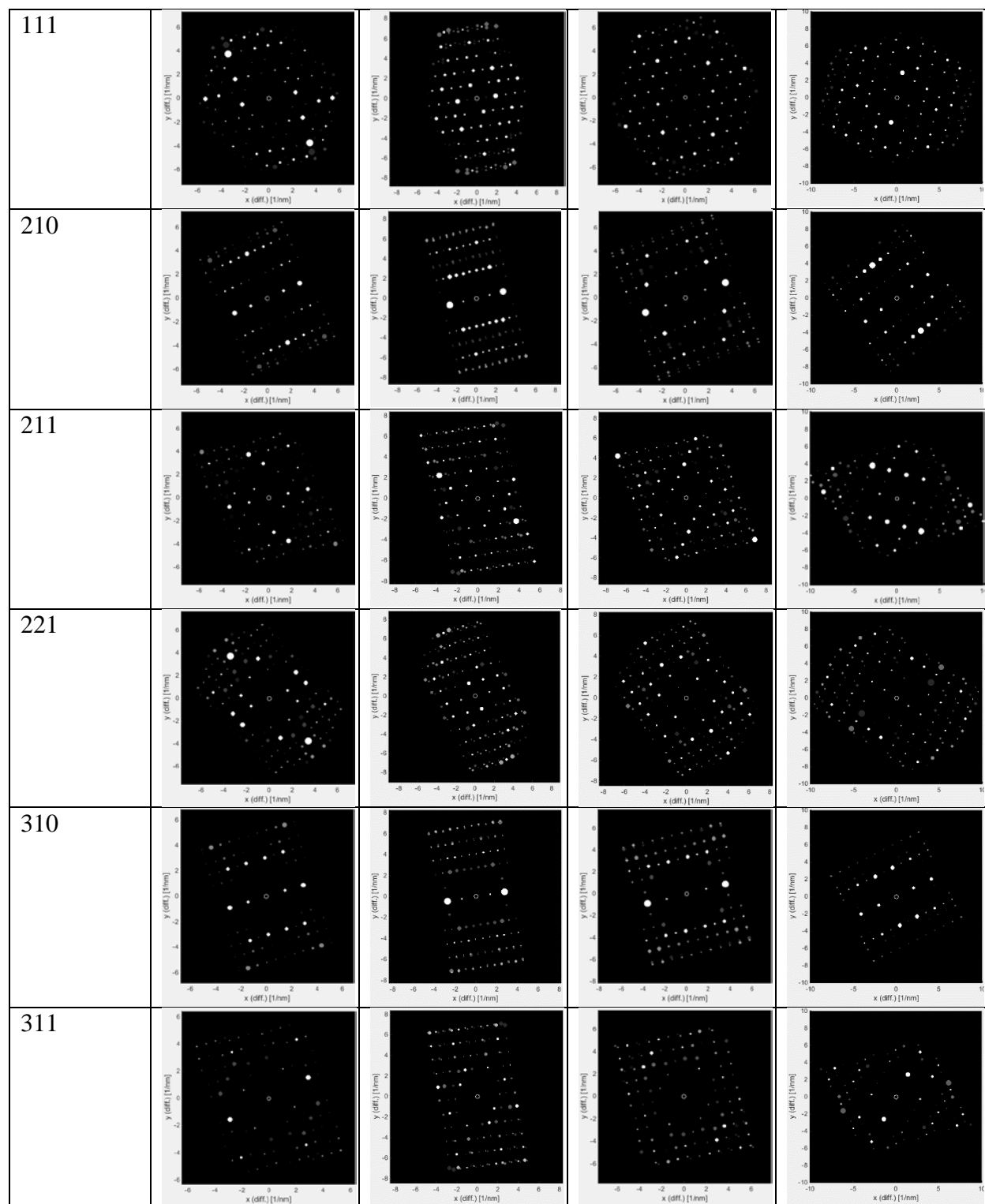
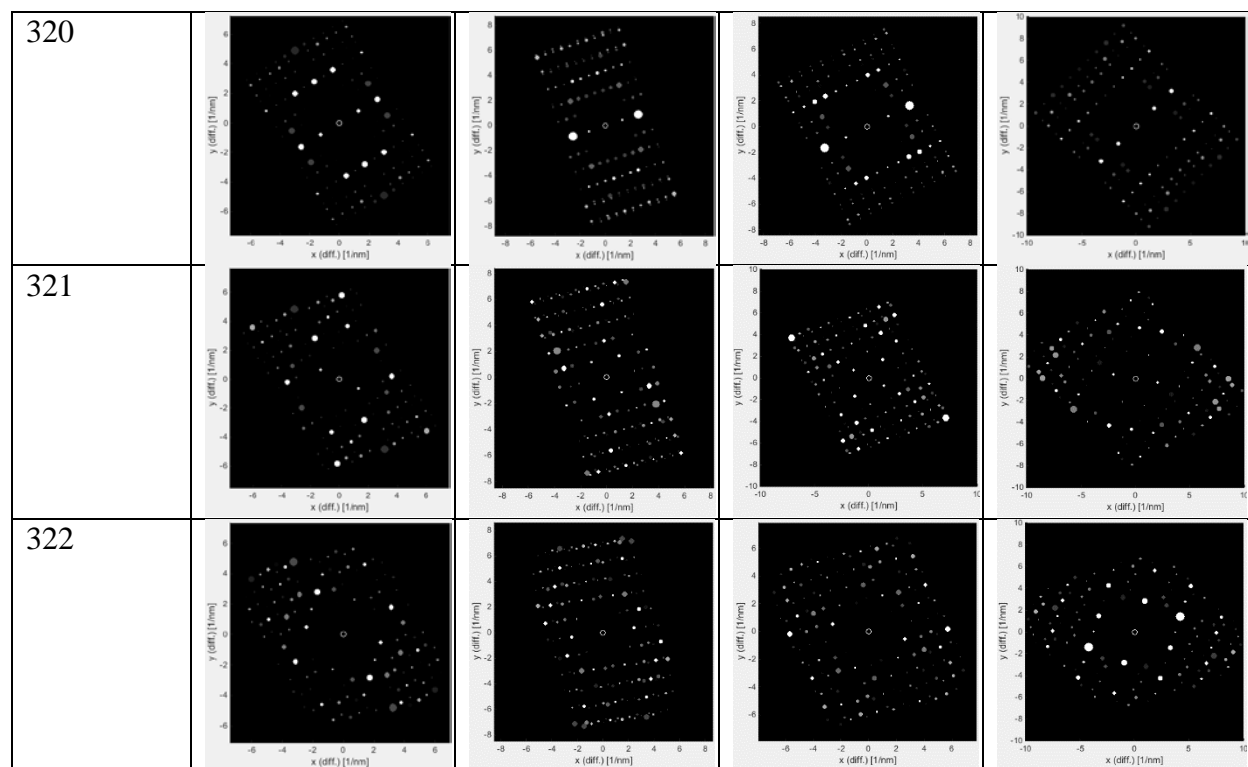


Table 6. Continued.



3.1.3 CL-20

The diffraction pattern of four polymorphs of CL-20 is simulated and shown below:

Table 7. Simulated DPs of CL-20 phases using CrystBOX.

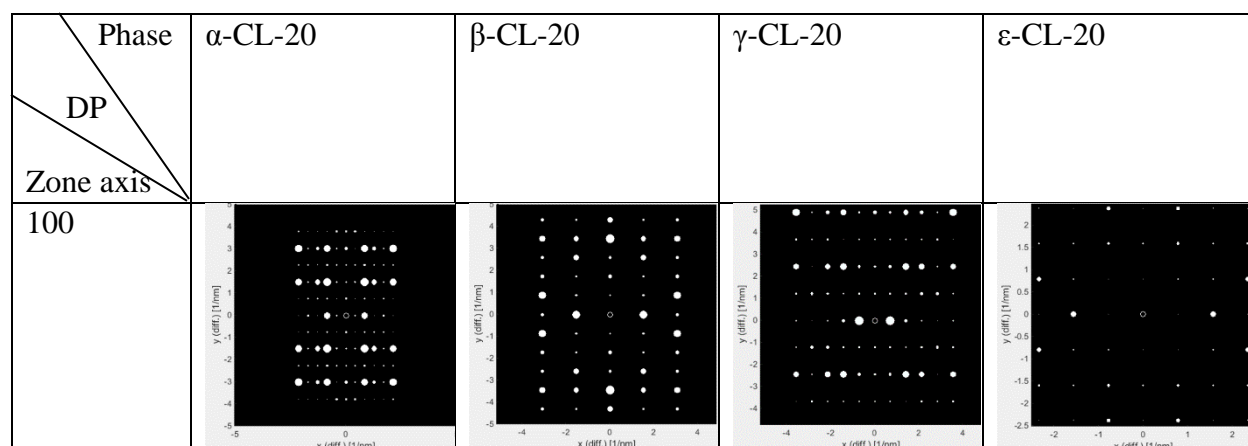


Table 7. Continued.

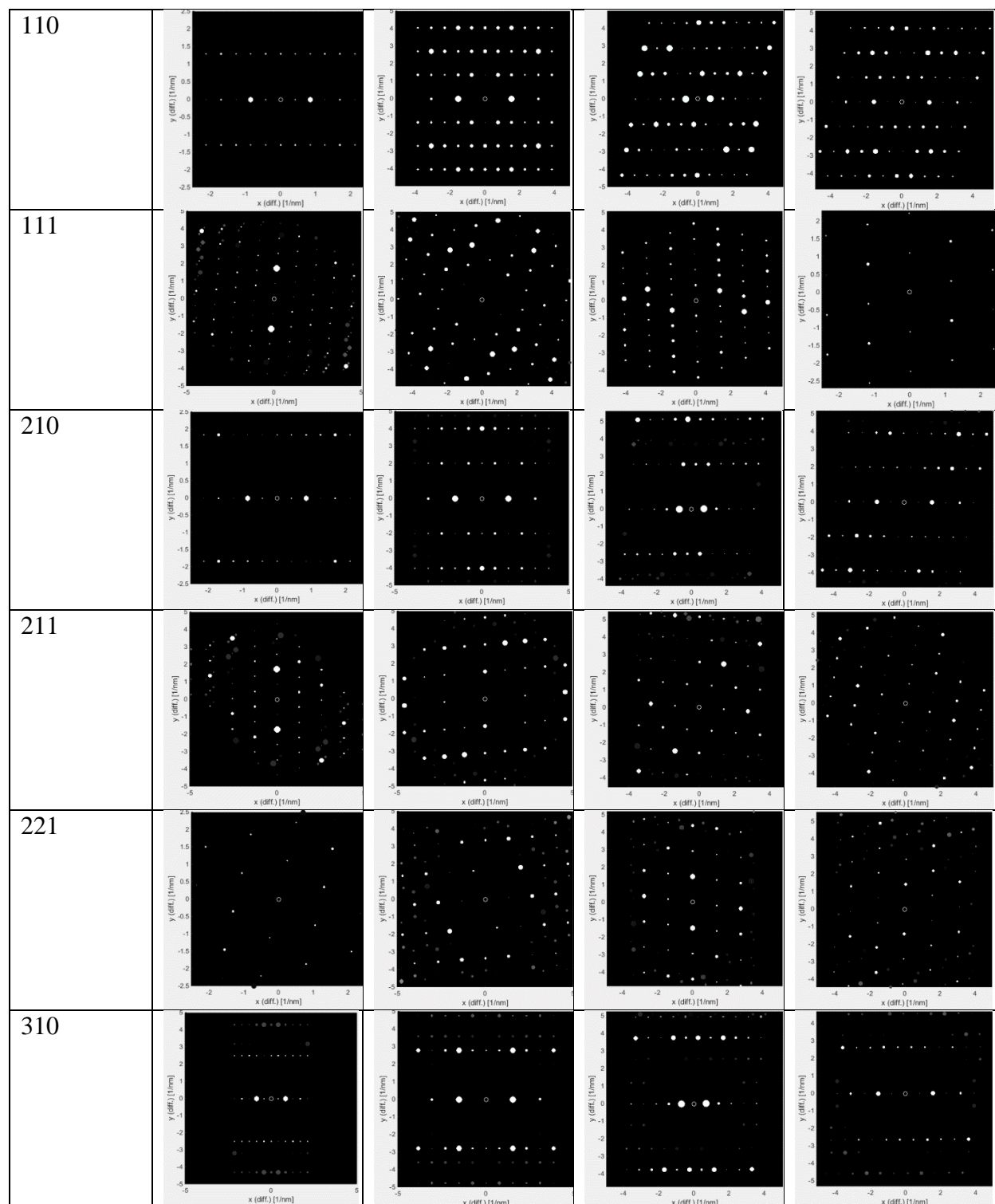
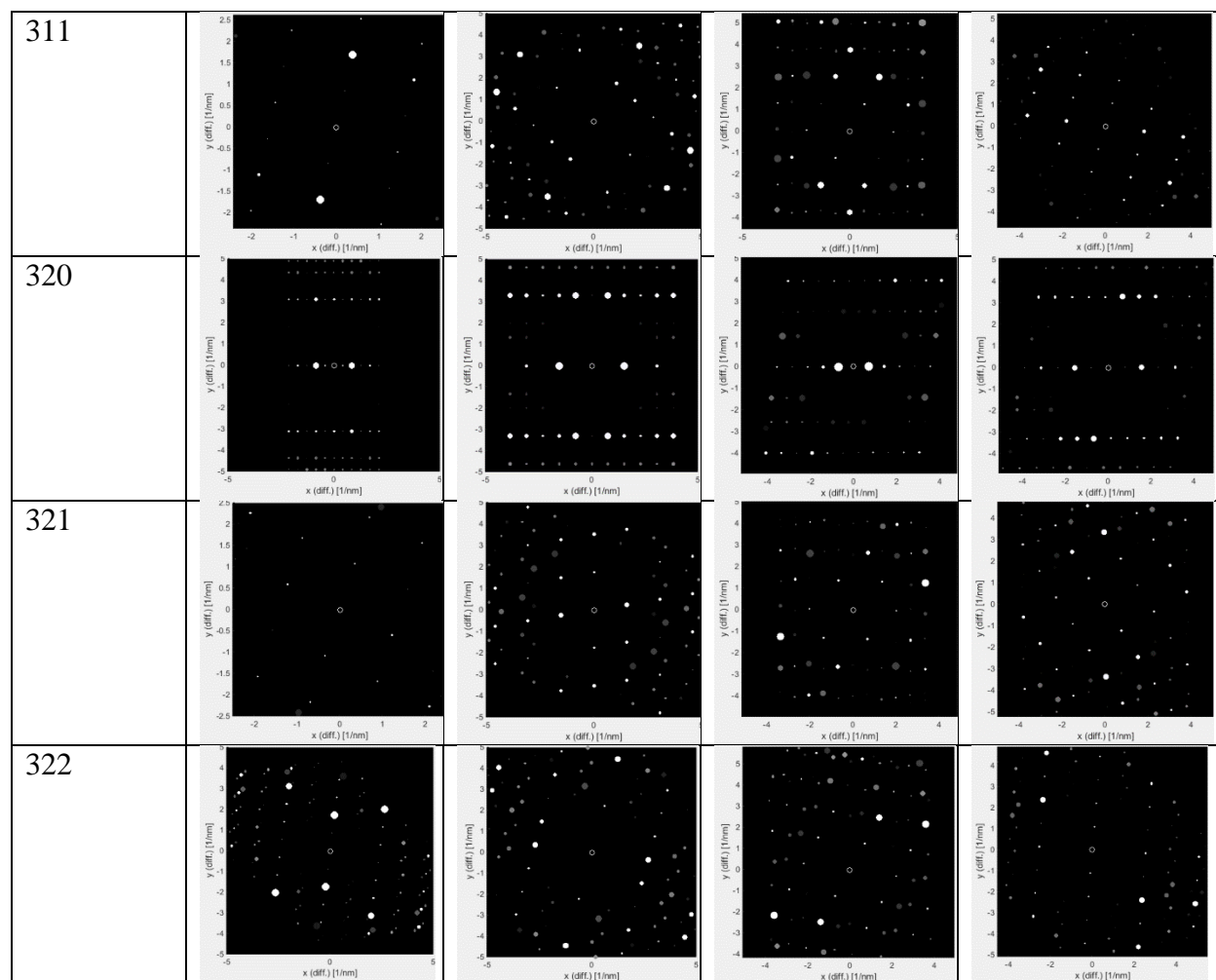


Table 7. Continued.



3.2 Investigation of HMX using UTEM and tomography

The HMX we have obtained in our lab was first mixed with acetone and then drop-casted onto the TEM grid for UTEM characterization. Careful examination reveals that HMX exists in multiple morphologies as shown in Figure 7. They can form flower-like clusters like in Figure 7a. Different contrast of the two big clusters in the image (denoted by the red arrows) is resulted from the variation in thickness. Figure 7b shows HMX in the form of flakes. The thickness and width of the HMX flakes also vary from position to position. There are also some HMX with strip-like structures as shown in Figure 7c and they are characterized by large aspect ratios.

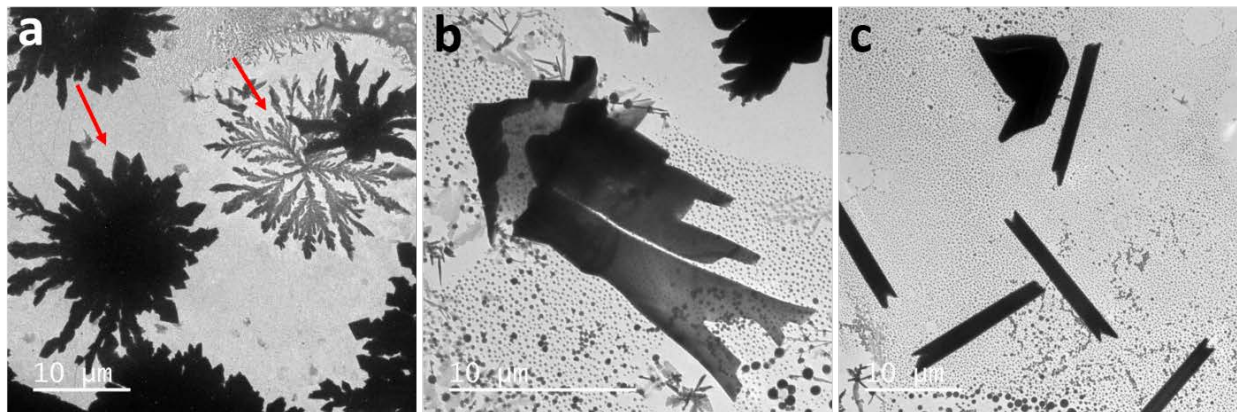


Figure 7. Bright field TEM images of HMX samples with different morphologies: (a) flower-like structures, (b) flakes and (c) strips.

It was found that HMX is very sensitive to both the laser beam and electron beam. Under the normal TEM imaging mode, even an electron beam with medium intensity to get a decent image would cause the degradation of the HMX sample. The degradation starts with the formation of small bubbles on the sample surface as shown in Figure 8a. If the electron beam or laser beam irradiation continues, those bubbles will grow both in size and numbers. A seriously damaged HMX sample is shown in Figure 8b, which is completely covered with bubbles. Therefore, a low electron beam intensity and a longer exposure time should be used for the imaging of HMX.

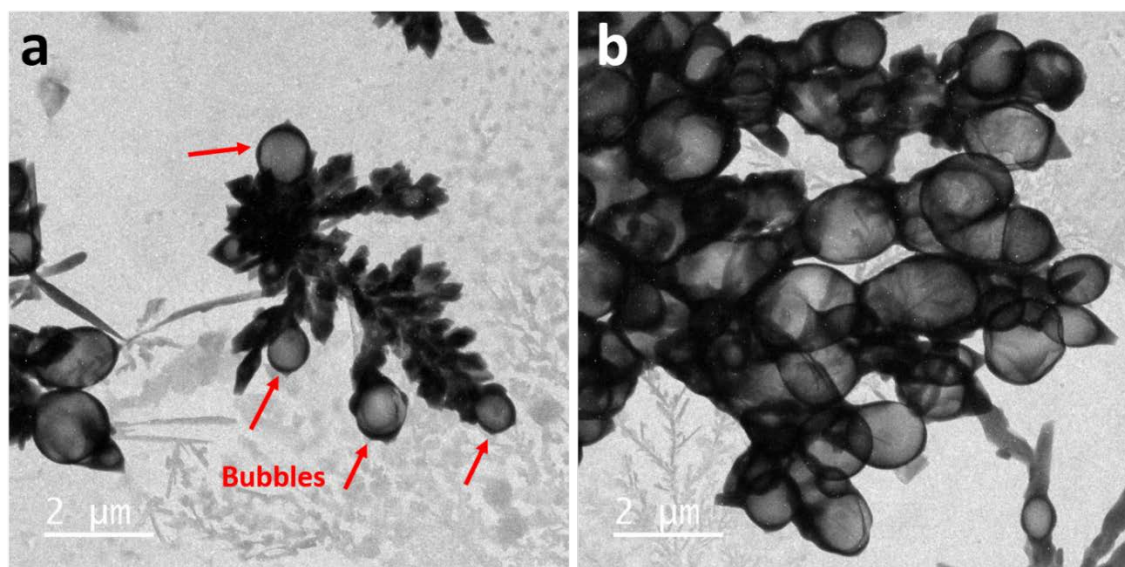


Figure 8. Bright field TEM images showing (a) a slightly degraded and (b) a seriously degraded HMX sample. The number and size of bubbles are increased with electron beam exposure.

Among the three morphologies of HMX shown in Figure 7, the stripped structure is the simplest and the most consistent one over a large sampling area. Therefore, we started our investigation on HMX from the strip-shaped samples. As mentioned before, HMX has three major phases including α -HMX, β -HMX and γ -HMX. So the first step of our investigation is to figure out which phase the strip-shaped HMX has. Selected area diffraction (SAD) was utilized to get diffraction patterns from multiple sample points, which were then compared and matched with simulated patterns shown in the previous section. Since HMX is very sensitive to even electron beams, it was really hard to get nice and clear diffraction patterns with beautiful contrast. The crystalline phase quickly degraded into amorphous phase, which resulted in a fast blurring of the sharp diffraction spots. Sometimes there is no time to insert the beam stopper in order to capture a decent diffraction pattern (Figure 9). To deal with this and protect the sample as much as possible, an extremely low-intensity electron beam and a long exposure time were used as a combination. Couple of diffraction patterns were obtained under such conditions, and the best two are shown in Figure 9a and 9c. After careful comparison and matching between the experimental diffraction patterns and simulated ones, it was revealed that our sample is most likely β -HMX since the diffraction patterns fit two of the simulated patterns of β -HMX under two specific zone axis quite well. (Figure 9b and 9d).

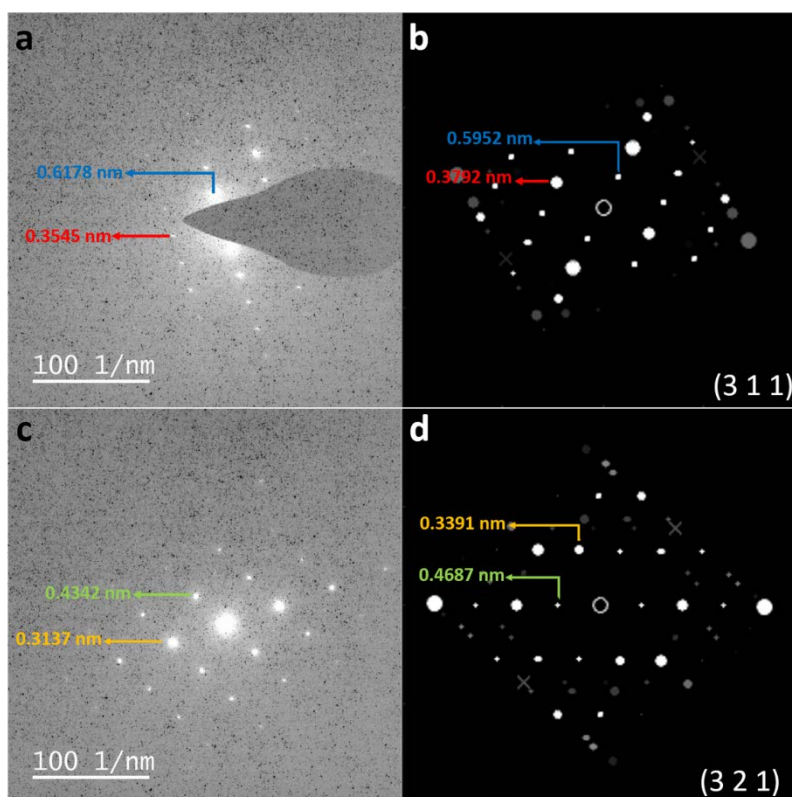


Figure 9. Selected area diffraction pattern of HMX from two different locations (a, c) and corresponding simulated patterns (b, d) respectively by CrysTBOX.

After the crystalline phase of HMX was determined, its three-dimensional (3D) structure was also reconstructed and examined. This is critical since the 3D structure might play an important role in determining the properties of HMX, especially considering that HMX can exist in several totally different morphologies. Therefore, it is necessary to demonstrate the 3D structure of HMX before any further investigation of HMX using UTEM. It seems that the structure of strip-shaped HMX is rather simple and straightforward which does not need any 3D demonstration. However, the point is to test if it is possible to do tomography using bright field UTEM images instead of the most commonly used HAADF-STEM images. Also, this is the first time for us to do tomography at micrometer level, which is a rather low magnification. The resulted 3D reconstruction is decent, as shown in Figure 10. The HMX bar at the center has a thickness at least the same as the reconstructed volume height. The small particles around, which are intentionally placed as fiducial markers, are also nicely reconstructed. This is a demonstration of our ability to

do tomography using normal bright field UTEM images, which will be helpful in the future for visualizing some complicated structures with confusing 2D images.

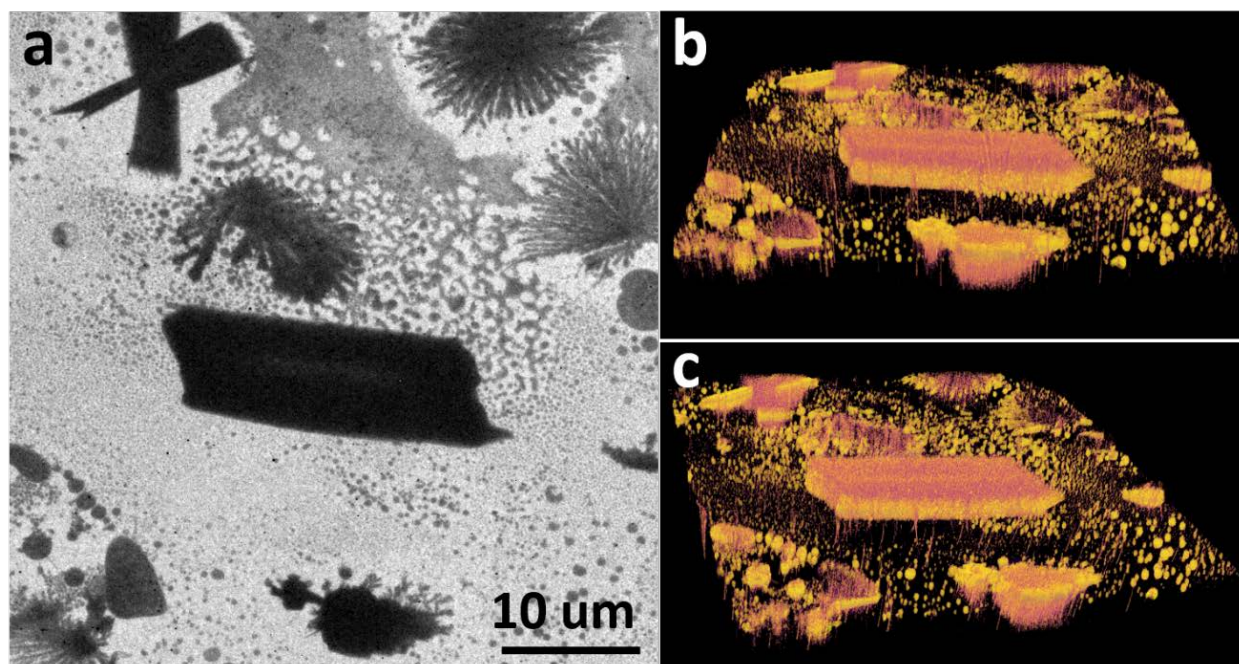


Figure 10. (a) Bright field TEM image of a strip-shaped HMX piece. (b, c) 3D reconstruction of the same region viewed from different directions.

CHAPTER 4. LASER-INDUCED WELDING OF PLASMONIC NANOSTRUCTURES

4.1 Laser-induced inter-welding and alloying of silver and gold nanoparticles⁹⁰

In this work, the welding between gold and silver NPs induced by a nanosecond pulsed laser was studied. UTEM was used to investigate the welding process at real time, which has never been reported before. Since we want to get a better understanding towards the welding process and involved mechanisms, two-nanoparticle welding was specifically studied as it is the simplest and most fundamental case which is also the first step to understand the welding of more complicated structures. We studied both the structural and compositional evolution of the Au-Ag NP pairs using UTEM, scanning transmission electron microscopy (STEM) and energy-dispersive X-ray spectroscopy (EDX). We also assessed the optical properties of the dimers after welding using the finite difference time domain (FDTD) method and found the welded dimers have unique optical responses compared to pure Ag-Ag and Au-Au dimers. This might provide useful information for the design of nanoparticle-based plasmonic devices with flexible optical responses.

4.1.1 Experimental methods

Ag colloid purchased from Sigma Aldrich (60 nm, aqueous buffer) and Au colloid purchased from Nanopartz (50 nm, DI water buffer) were mixed with a 1:1 ratio. The mixed solution was dispersed onto a carbon-coated copper grid. *In situ* laser experiments were performed using an ultrafast transmission electron microscope (UTEM) based on a FEI Tecnai G20 system. A Nd-YAG pulsed laser with a wavelength of 532 nm, frequency of 25 kHz, pulse width of 1 ns and $1/e^2$ spot size of 120 μm was used as the sample excitation laser. different laser power was used in the experiments, ranging from 0.4 mW to 3 mW. The sample excitation laser was set at duty cycle mode by an external delay generator. In a duty cycle mode, some off-pulses are put between a specific number of on-pulses in each cycle in order to reduce the sample vibration thus record videos with higher quality.

NPs after laser irradiation were characterized by high angle annular dark-field scanning transmission electron microscopy (HAADF-STEM) and energy-dispersive X-ray spectroscopy (EDX) using FEI Titan EFTEM 80-300 kV. Both mapping and linescan were used during EDX analysis. The FDTD simulation was performed using the open source software MEEP.⁸⁸ A

Gaussian electromagnetic source with a central frequency of 660 THz and a frequency span of 720 THz was used and the electric field was polarized along the longitudinal direction of dimers. The absorption efficiency of several types of dimers formed after welding experiment as described in the following results was simulated and compared with each other. All the dimers were simulated with a NP overlapping distance of 4nm to represent welding. To study the effect of composition, dimers were simulated in the same geometry, namely, a 60nm-sized NP and a 50nm-sized NP. Specifically, in the simulation of the Ag-Au@Ag dimer, the thickness of the Ag envelope is chosen to be 2 nm based on experimental observation. To study the effect of NP size ratio, a dimer with equally sized Au and Ag NPs (50nm) was calculated and compared with the previous Ag-Au dimer.

4.1.2 Results and discussion

To see how the morphology or structure of a Ag-Au NP pair changes under the condition of laser irradiation, a series of TEM images were taken after different number of pulses or different laser irradiation time length inside the UTEM. The results are shown in Figure 11. As we can see, with increasing laser irradiation time, a neck first forms between two NPs and then grows, which is an indicator of localized heating at the interparticle gap, known as a ‘hotspot’ effect.⁹¹ As exposed to increasing laser pulses, the neck grows via surface diffusion in order to reduce the total surface area and the large curvature difference at the gap.⁹² In principle, two nanoparticles should merge into one completely in order to minimize the total surface energy.⁹³ However, that is rarely observed in our experiment. To explain this partial joining, two factors must be considered. The first one is the limitation of laser power. In our experiment, the laser power used is very low as we want to capture as many details of the welding process as possible. As a result, the rate of particle coalescence is strongly limited. The second reason is related to the driving force of nanoparticle joining. As the surface area of the NP dimer keeps decreasing under laser irradiation, the driving force for coalescence also decreases. As a result, the coalescence process becomes slower and slower. This is further proved by the decreasing rate of neck growth as shown in Figure 11. So our conclusion is that, although a complete coalescence can be achieved theoretically, it needs a sufficiently long time considering the suppressed laser power.

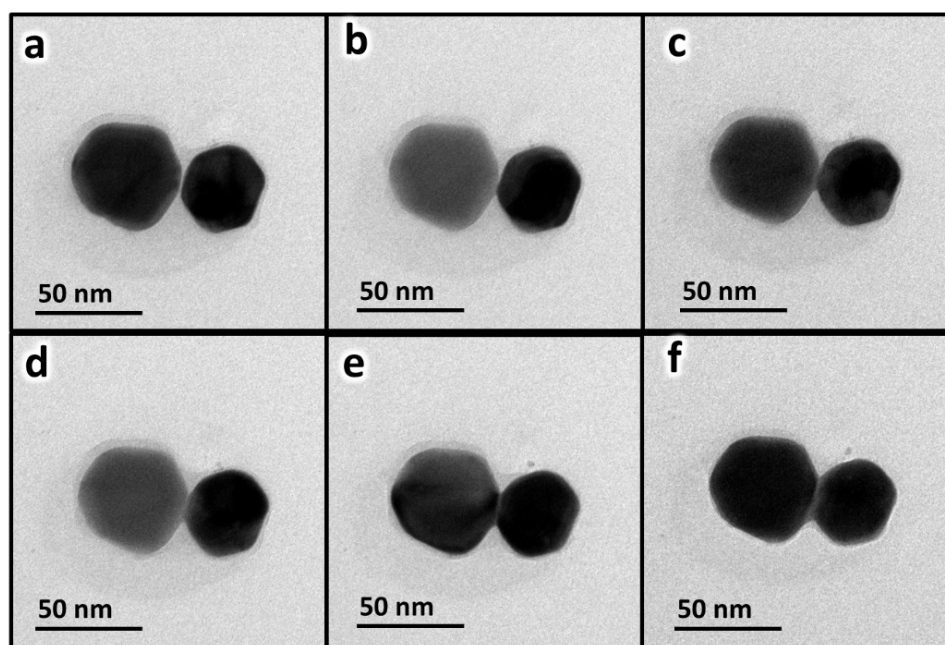


Figure 11. Bright field TEM images of a NP dimer before laser exposure (a) and after being exposed to pulsed laser for 2s (b), 10s (c), 20s (d), 100s (e) and 1000s (f). A duty cycle mode was used with 10 laser pulses on and 90 pulses off in each cycle. Laser power was 0.4mW.

To check compositions of the Ag-Au NP dimers after laser experiments, the sample was characterized by STEM imaging and EDX mapping. The STEM imaging uses a high angle annular dark field (HAADF) detector which gives good contrast between elements of different atomic numbers.⁹⁴ In the STEM images, Au NPs are brighter than Ag NPs because elements with higher atomic number have more electrons scattered to high angles. After checking the composition of numerous dimers, we found that all of them belong to four basic configurations as shown in Figure 12: In Figure 12a, the Au NP and the Ag NP are connected by a small neck without notable interdiffusion between them. In Figure 12b, the Au NP is wrapped up by a thin silver layer. In Figure 12c, a gold shell is formed around the Ag NP, connected with an Au/Ag alloy NP. In Figure 12d, more gold atoms have migrated into the Ag NP and they have started to diffuse and mix with the inside Ag NP, indicating an alloying process. To the best of our knowledge, this is the first time that the intermediate stages of the welding between Ag and Au NPs are detected before the formation of a final alloy.

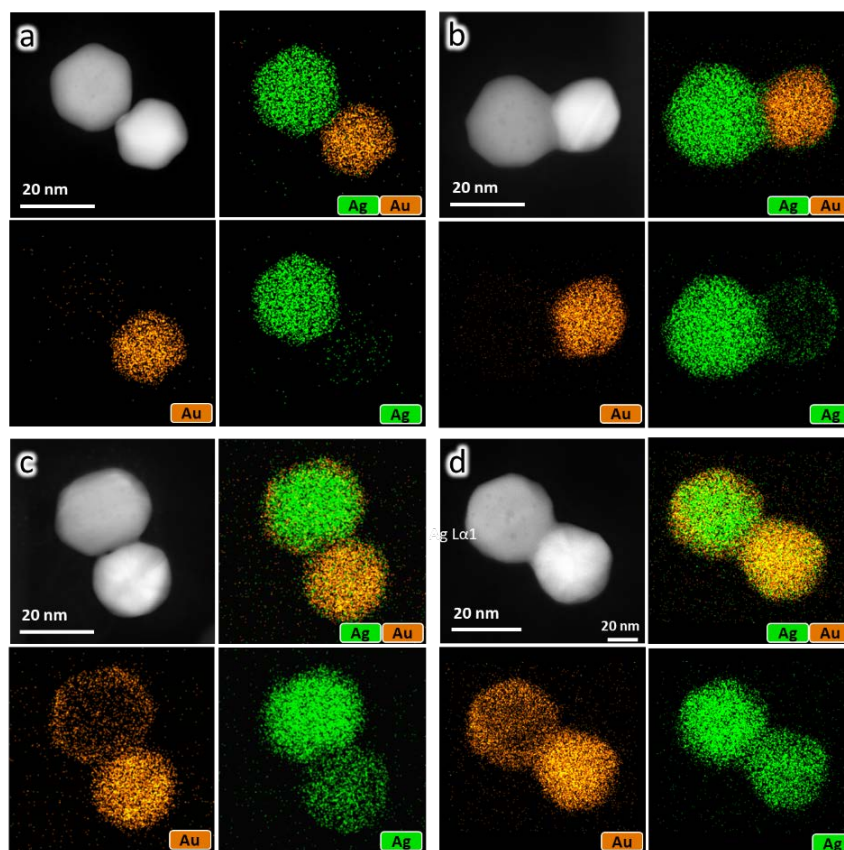


Figure 12. HAADF-STEM images of Ag-Au NP dimers and corresponding EDX mapping.

Based on the structures observed above, the welding of Au-Ag NPs can be divided into five distinct stages: Neck formation, silver shell formation, gold shell formation, alloy dimer formation and single alloy NP formation. The neck formation is induced by the localized heating at the inter-particle gap, as discussed before. After the neck is formed, the localized heating moves along the seam formed by the welding, which leads to the growth of neck.²² During this process, surface diffusion plays an important role in transporting materials from NPs the neck region. The formation of a silver shell can be explained from the perspective of energy. It has been reported that the surface energy of Ag crystals (1.25 J/m^2)⁹⁵ is smaller than that of the Au crystals (1.50 J/m^2)⁹⁶. Therefore, it leads to an energy reduction if the Au NP surface is enveloped by the Ag. Furthermore, it is well known that silver has better structural adaptability than Au, meaning that Ag is “softer” than Au. It has been observed in a previous study⁹⁷ that a silver NP would wet a gold NP on contact and wrap it up whereas the gold NP remains almost unchanged. This happens irrespective of which nanoparticle is larger, as illustrated in Figure 13a and 13b, which cannot be

explained by the well-established Ostwald ripening theory. The ‘softness’ of silver is even more clear in Figure 13c: two Au NPs are wrapped up together by the same Ag shell originating from the same Ag NP.

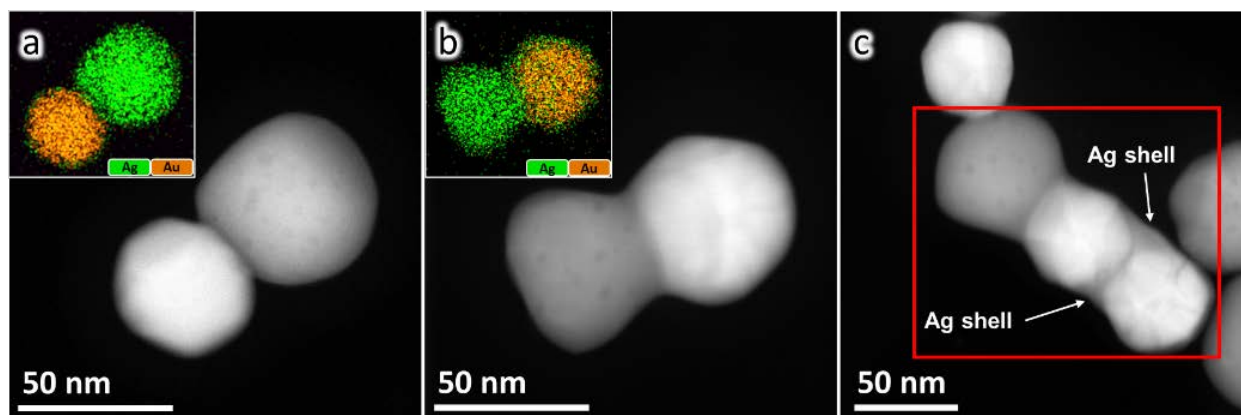


Figure 13. HAADF-STEM images and EDX mapping showing Ag wrapping up Au NPs when (a) Ag NP is larger than Au NP and (b) Ag NP is smaller than Au NP. In (c), the Ag NP in the red square wraps up two Au NPs.

In the third stage, the Au@Ag core-shell NP formed in the previous stage transformed into an Ag/Au alloy. At the same time, the pure Ag NP is surrounded by a very thin Au layer, as shown in Figure 12c. For the alloying of the Au@Ag core-shell NP, it has been studied before^{98–100} and we believe that two important mechanisms are involved. One is the surface melting mechanism, meaning that the low melting point of Ag at the core-shell NP surface leads to surface melting which greatly accelerated diffusion.⁹⁸ The other mechanism is the vacancy mechanism: there are vacancies or other lattice defects at the core-shell interface which provides active site for interdiffusion to happen.⁹⁹ The formation of the Au shell is an important implication of the interdiffusion between Au and Ag NPs. This can be understood from a thermodynamic perspective. It has been reported that there is an energy gain of 0.36eV in forming an Ag-Au bond by breaking Au-Au and Ag-Ag bonds.⁹⁷ Therefore, it is energetically favorable to form an Au/Ag alloy. However, there is a kinetic barrier for the formation of Au/Ag alloy out of pure Au and Ag. In our experiments, the kinetic barrier is compensated by the energy provided by the pulsed laser, which makes the alloying process much easier and more accessible. As a result, the diffusion of Au towards the Ag NP is accelerated. Au atoms prefer to diffuse along the surface of the Ag NP since the Ag atoms at surface are more energetic and active than those in the interior.

In the fourth stage, the Ag@Au core-shell structure described above also transforms into an Au/Ag alloy (Figure 12d). We infer that this is also related to the defects at the core-shell interface. Up to now, both NPs in the dimer have become alloys. In principle, those two NPs will merge one NP considering that Au and Ag are completely intermiscible and the system tends to minimize the total surface area. We define the formation of a single NP as the fifth stage. However, as mentioned before, NPs in this stage are barely observed as it takes a long time to achieve a complete merging and alloying.

The optical property of the NP dimers formed in the first and second stage (denoted as Ag-Au dimer and Ag-Au@Ag dimer respectively) were examined using three-dimensional (3D) finite difference time domain (FDTD) method. Pure Ag and Au NP dimers were also simulated as comparison. The absorption efficiency was calculated to represent the overall optical properties of NP dimers. This is reasonable as the extinction of Au or Ag NPs with a size around 50 nm is dominated by absorption. All dimers simulated in Figure 14a have the same geometry as shown in Figure 14a inset. Specifically, for the Ag-Au@Ag dimer, the Ag shell thickness is set to be 2 nm to match with the experimental observation. As shown in Figure 14a, there is a dominant resonance peak in the near-infrared region for all the four dimers simulated, which corresponds to the long-wavelength dipolar mode.^{32,101} Other mild peaks at shorter wavelengths corresponds to some higher-order plasmon modes. Both the Ag-Au dimer and Ag-Au@Ag dimer have their dipolar resonance peaks between that of pure Ag-Ag and Au-Au dimers. The effect of NP size ratio in the dimer was also examined and we found that changing the relative size of Au and Ag NP also changes the LSPR behavior of the dimer they formed (Figure 14b). From the results above, we can see that the inter-welding of Ag and Au NPs results in dimers with LSPR behaviors that are different from pure Ag and pure Au dimers. Also, changing the size ratio of Ag and Au NPs makes it possible to further tune the optical responses of Ag-Au NP dimers.

In conclusion, we investigated both the structural and compositional evolution of Ag-Au dimers during laser irradiation and found the intermediate structures before the formation of Ag/Au alloy. Combining the experimental condition and previous theory on the welding of Ag-Au structures, we explained the formation mechanism of each structure. What we found in this work might provide new ideas for the fabrication of novel plasmonic devices with unique LSPR properties. Again, UTEM proved to be a powerful tool for the systematical study of laser-induced material transformations.

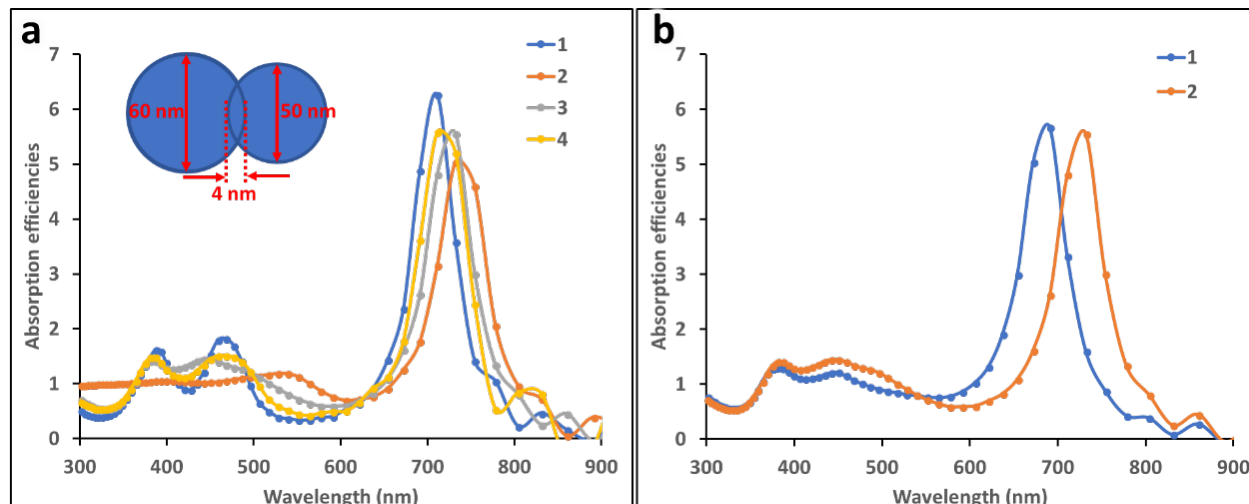


Figure 14. (a) Absorption efficiencies of four types of dimers: 1. Ag NP (60nm) + Ag NP (50nm), 2. Au NP (60nm) + Au NP (50nm), 3. Ag NP (60nm) + Au NP (50nm), 4. Ag NP (60nm) + Au@Ag core-shell NP with a core size of 46nm and shell thickness of 2nm. (b) Comparison of the absorption efficiencies of Ag-Au NP dimers with different Ag NP sizes but the same Au NP size. Curve 1: Ag NP (50nm) + Au NP (50nm) with a 4nm overlapping; curve 2: Ag NP (60nm) + Au NP (50nm) with a 4nm overlapping.

Aside from the welding between Au and Ag NPs, we also studied laser-induced welding of other plasmonic nanostructures, which is shortly introduced in the next two sections.

4.2 Laser-induced welding of silver nanowires¹

Silver nanowires have been widely studied due to their application in nanoelectronics as circuit elements or interconnects. Ag nanowire network with both low resistance and high transparency is very promising in replacing the conventional transparent conductor film material indium tin oxide (ITO). In this work, a pulsed laser was used to induce welding between silver nanowires inside the UTEM. The welding process was directly visualized through which a better understanding towards the welding mechanism was obtained.

Silver nanowires purchased from Sigma Aldrich (diameter 115 nm, Length 20-50 μm) was exposed to an excitation laser which is a frequency-doubled Nd-YAG nanosecond pulsed laser with a wavelength of 532 nm and frequency of 25 kHz inside UTEM. Laser power ranging from 5 mW to 100 mW was used. The time evolution of nanowire junctions under laser irradiation was

¹ Data used in this section is included in a paper under preparation.

captured inside UTEM, as shown in Figure 15. It is clear that, at the crossing point of two nanowires, they were welded together with the formation of ligaments first. Subsequent laser pulses result in the formation of a neck in one of the branches (see image below) while the other branches remain unchanged. Further irradiation makes the neck narrow down from both ends and finally, a nanogap is formed as the neck pinches off. To study the crystal orientation at nanowire junctions, selected area electron diffraction (SAED) patterns were taken from multiple junctions as shown in Figure 16. The diffraction patterns (DP) from the junction shows mainly one set of spots that are consistent with the DP from the thicker Ag nanowire, indicating that the junction has adopted the crystal orientation of the thicker nanowire. This is reasonable since there are less materials from the thinner nanowire at the junction thus it costs less energy for atoms from the thinner nanowire to reorient. In order to figure out if it is always the thinner nanowire merging into the thicker one no matter which nanowire is on top, SEM imaging and three dimensional reconstructions were also done, which will not be discussed here. Nevertheless, it was finally proved that it is the thinner nanowire, rather than the nanowire at the bottom, that contributes to welding and adopts the crystal orientation of the thicker nanowire at the junction.

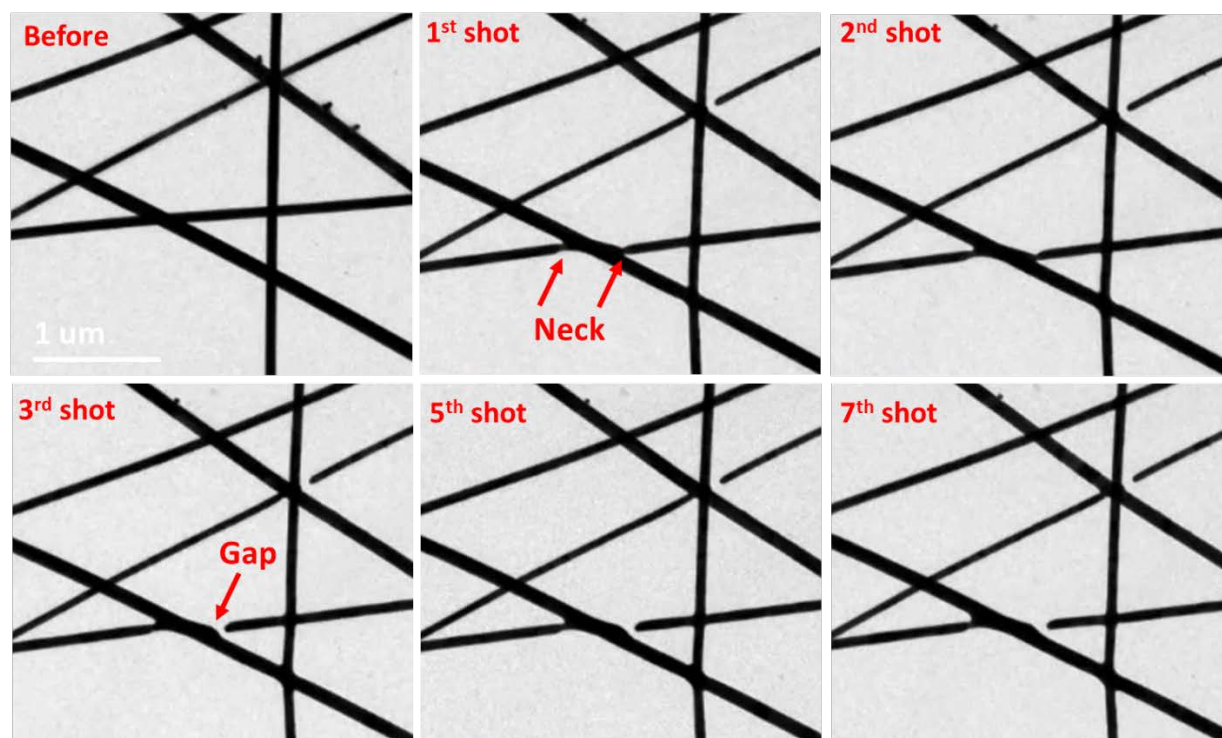


Figure 15. Bright field TEM images of a silver nanowire junction after different number of laser pulses.

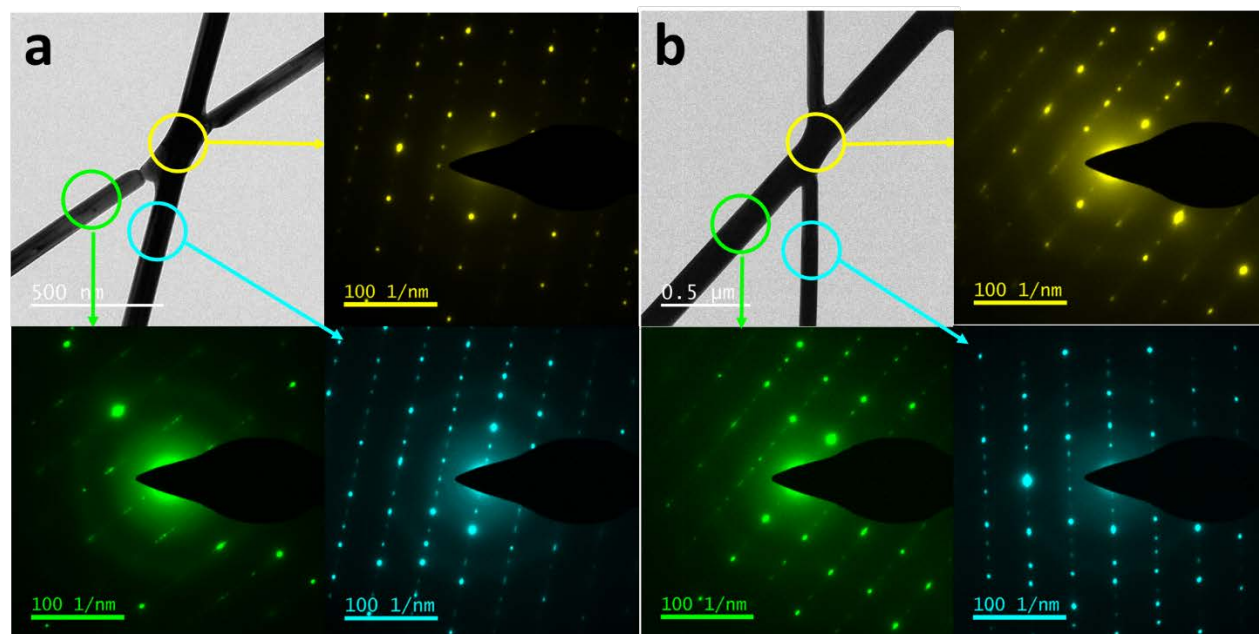


Figure 16. Bright field TEM images of two Ag NW junctions after laser irradiation and diffraction patterns from different regions (shown by the arrows) of the NWs.

4.3 Laser-induced merging of gold nanoparticles into silver nanowires²

Noble metallic nanocomposites with controlled morphology and composition have been widely studied due to their applications in catalysis, plasmonics, optics, biologics, etc. One way to form metallic composite is to join metal components with different geometries. In this study, we chose two types of nanostructures, namely, Ag nanowire and Au nanoparticle. By merging Au nanoparticles into Ag nanowires, it might be possible to obtain nanowires with special optical and chemical properties.¹⁰² Therefore, we conducted *in situ* laser irradiation experiments to investigate the welding and merging of Au nanoparticles into Ag nanowires using UTEM and characterized the resulting structures.

The Ag nanowires (average diameter of 115 nm) and Au NPs (average diameter of 50 nm) were mixed and then used for laser irradiation experiments inside UTEM, with the same sample excitation laser described before. Laser power ranging from 10 mW to 100 mW was used to induce the welding. Again, the time evolution of the nanostructures during welding were captured by UTEM as shown in Figure 17. As we can see, the Au NPs are bridged with the Ag NW after being exposed to laser. Since we cannot differentiate between Ag and Au under TEM mode, the

² Data used in this section has been included in a paper under preparation.

compositional evolution of the welded composite was checked using HAADF-STEM imaging and EDS after laser experiments. EDX mappings from multiple regions reveal three distinct structures after laser experiments, as shown in Figure 18. Based on this, the welding process can be divided into three stages, similar to the idea used in Section 4.1. Firstly, contacts between the Ag NW and Au NPs are established and Ag forms cup-like shapes below the Au NPs as indicated by the purple arrows. Secondly, the contact angle between the Ag NW and Au NP becomes smaller and a shell-like structure of Ag was formed over the Au NP. At last, more Au diffuse into the Ag NW leading to an alloyed NW structure. Analogous to the welding between Ag and Au NPs, we also studied the mechanisms involved in the three stages from the perspective of diffusion and thermodynamics. In conclusion, we believe that the understanding obtained in this study might provide useful information for the joining of different nanomaterials to creating nanocomposites with controlled morphology and composition.

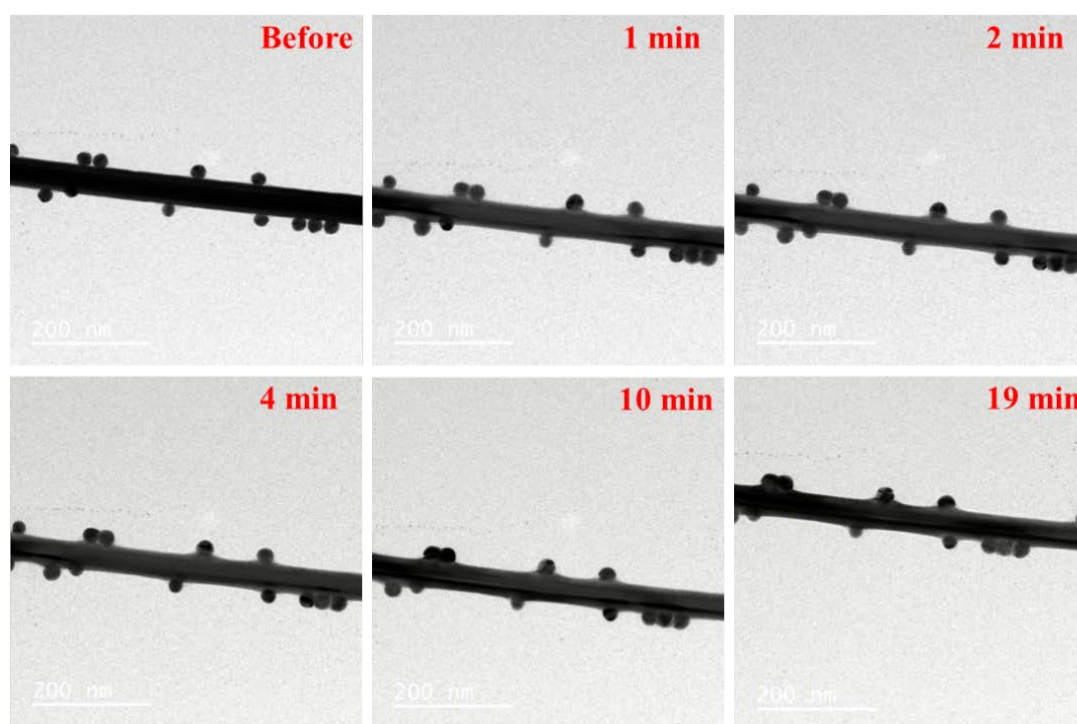


Figure 17. Real-time visualization of the merging of Au NPs into the Ag NW.

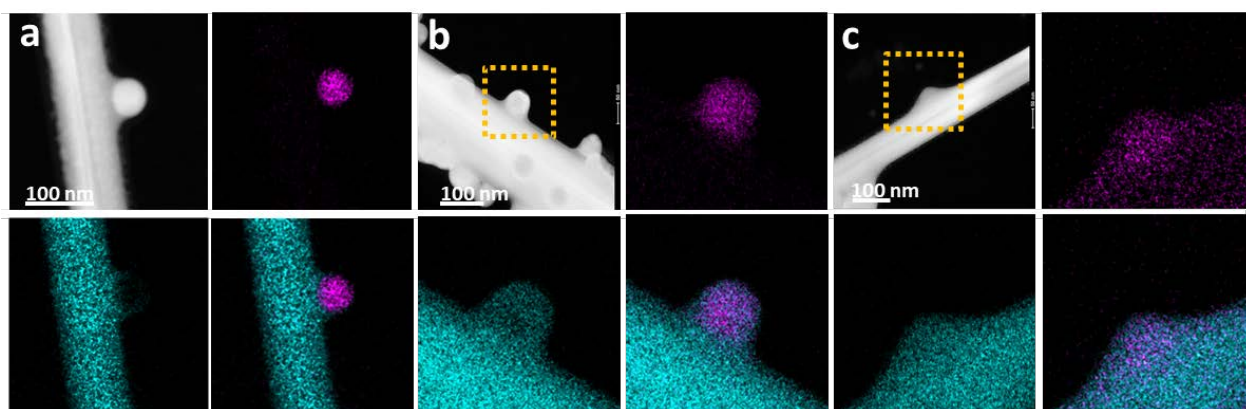


Figure 18. HAADF-STEM images and EDS maps of Ag and Au showing different stages of the merging process as described in the text.

REFERENCES

1. Breinan, E. M., Banas, C. M. & Kear, B. H. Processing materials with lasers. *Phys. Today* 29, 44–48 (1976).
2. Hong, K.-M. & Shin, Y. C. Prospects of laser welding technology in the automotive industry: A review. *J. Mater. Process. Technol.* 245, 46–69 (2017).
3. Wang, H., Lin, H., Wang, C., Zheng, L. & Hu, X. Laser drilling of structural ceramics: A review. *J. Eur. Ceram. Soc.* 37, 1157–1173 (2017).
4. Costa Rodrigues, G., Cuypers, M., Fallahi Sichani, E., Kellens, K. & Duflou, J. R. Laser cutting with direct diode laser. in *Physics Procedia* 41, 558–565 (2013).
5. Yu, P. & Zeng, Y. Characterization of laser-induced local heating in a substrate. *J. Heat Mass Transf.* 106, 989–996 (2017).
6. Terakawa, M. et al. Femtosecond laser direct writing of metal microstructure in a stretchable poly(ethylene glycol) diacrylate (PEGDA) hydrogel. *Opt. Lett.* 41, 1392–1395 (2016).
7. Jin, R. et al. Controlling anisotropic nanoparticle growth through plasmon excitation. *Nature* 425, 487–490 (2003).
8. Jiao, Z. et al. Nanostructure evolution in joining of Al and Fe nanoparticles with femtosecond laser irradiation. *J. Appl. Phys.* 115, (2014).
9. Hu, A. et al. Femtosecond laser welded nanostructures and plasmonic devices. *J. Laser Appl.* 24, 042001 (2012).
10. von Allmen, M. & Blatter, A. *Laser-Beam Interactions with Materials*. Springer Series in Materials Science (1995). doi:10.1007/978-3-642-57813-7
11. Lobastov, V. A., Srinivasan, R. & Zewail, A. H. Four-dimensional ultrafast electron microscopy. *Proc. Natl. Acad. Sci. U. S. A.* 102, 7069–73 (2005).
12. Shorokhov, D. & Zewail, A. H. Perspective: 4D ultrafast electron microscopy—Evolutions and revolutions. *J. Chem. Phys.* J. Chem. Phys. J. Chem. Phys. J. Appl. Phys. J. Chem. Phys. 144, 80901–124706 (2016).
13. Grinolds, M. S., Lobastov, V. A., Weissenrieder, J. & Zewail, A. H. Four-dimensional ultrafast electron microscopy of phase transitions. *Proc. Natl. Acad. Sci.* 103, 18427–18431 (2006).
14. Bostanjoglo, O. High-speed electron microscopy. *Adv. Imaging Electron Phys.* 121, 1–51 (2002).

15. Zewail, A. H. Four-Dimensional Electron Microscopy. *Science* (80-.). 328, 187–193 (2010).
16. Strachan, D. R. et al. Real-Time TEM Imaging of the Formation of Crystalline Nanoscale Gaps. *Phys. Rev. Lett.* 100, 56805 (2008).
17. Dai, S. et al. Laser-induced single point nanowelding of silver nanowires. *Appl. Phys. Lett.* 108, (2016).
18. Xu, S. et al. Nanometer-Scale Modification and Welding of Silicon and Metallic Nanowires with a High-Intensity Electron Beam. *Small* 1, 1221–1229 (2005).
19. Wu, H. et al. A transparent electrode based on a metal nanotrough network. *Nat. Nanotechnol.* 8, 421 (2013).
20. Zhu, R. et al. Fused Silver Nanowires with Metal Oxide Nanoparticles and Organic Polymers for Highly Transparent Conductors. *ACS Nano* 5, 9877–9882 (2011).
21. Chen, H. et al. Transmission-electron-microscopy study on fivefold twinned silver nanorods. *J. Phys. Chem. B* 108, 12038–12043 (2004).
22. Garnett, E. C. et al. Self-limited plasmonic welding of silver nanowire junctions. *Nat. Mater.* 11, 241–9 (2012).
23. Hwan Park, J. et al. Flash-Induced Self- Limited Plasmonic Welding of Silver Nanowire Network for Transparent Flexible Energy Harvester. *Adv. Mater.* 29, 1603473 (2017).
24. Spechler, J. A. & Arnold, C. B. Direct-write pulsed laser processed silver nanowire networks for transparent conducting electrodes. *Appl Phys A* 108, 25–28 (2012).
25. Anker, J. N. et al. Biosensing with plasmonic nanosensors. *Nat. Mater.* 7, 442–453 (2008).
26. Sokolov, K. et al. Real-time vital optical imaging of precancer using anti-epidermal growth factor receptor antibodies conjugated to gold nanoparticles. *Cancer Res.* 63, 1999–2004 (2003).
27. El-Sayed, I. H., Huang, X. & El-Sayed, M. A. Selective laser photo-thermal therapy of epithelial carcinoma using anti-EGFR antibody conjugated gold nanoparticles. *Cancer Lett.* 239, 129–135 (2006).
28. Ozbay, E. Plasmonics: Merging Photonics and Electronics at Nanoscale Dimensions. *Science* (80-.). 311, 189–193 (2006).
29. Kelly, K. L., Coronado, E., Zhao, L. L. & Schatz, G. C. The Optical Properties of Metal Nanoparticles: The Influence of Size, Shape, and Dielectric Environment. *J. Phys. Chem. B* 107, 668–677 (2003).

30. Jackson, J. B. & Halas, N. J. Silver Nanoshells: Variations in Morphologies and Optical Properties. *J. Phys. Chem. B* 105, 2743–2746 (2001).
31. Graf, C., Vossen, D. L. J., Imhof, A. & Van Blaaderen, A. A general method to coat colloidal particles with silica. *Langmuir* 19, 6693–6700 (2003).
32. Zhang, T. et al. Plasmonic Properties of Welded Metal Nanoparticles. *Open Surf. Sci. J.* 3, 76–81 (2011).
33. Kim, S. J. & Jang, D. J. Laser-induced nanowelding of gold nanoparticles. *Appl. Phys. Lett.* 86, 1–3 (2005).
34. Borys, N. J., Shafran, E. & Lupton, J. M. Surface plasmon delocalization in silver nanoparticle aggregates revealed by subdiffraction supercontinuum hot spots. *Sci. Rep.* 3, 2090 (2013).
35. Fernanda Cardinal, M., Rodríguez-González, B., Alvarez-Puebla, R. A., Pérez-Juste, J. & Liz-Marzán, L. M. Modulation of localized surface plasmons and SERS response in gold dumbbells through silver coating. *J. Phys. Chem. C* 114, 10417–10423 (2010).
36. Walter, E. C., Murray, B. J., Favier, F. & Penner, R. M. “Beaded” Bimetallic Nanowires: Wiring Nanoparticles of Metal 1 Using Nanowires of Metal 2. *Adv. Mater.* 15, 396–399 (2003).
37. Wang, J. Barcoded metal nanowires. *J. Mater. Chem.* 18, 4017–4020 (2008).
38. Nicewarner-Peña, S. R., Carado, A. J., Shale, K. E. & Keating, C. D. Barcoded metal nanowires: optical reflectivity and patterned fluorescence. *J. Phys. Chem. B* 107, 7360–7367 (2003).
39. Liu, K., Nagodawithana, K., Searson, P. C. & Chien, C. L. Perpendicular giant magnetoresistance of multilayered Co/Cu nanowires. *Phys. Rev. B* 51, 7381–7384 (1995).
40. Blondel, A., Meier, J. P., Doudin, B. & Ansermet, J. Giant magnetoresistance of nanowires of multilayers. *Appl. Phys. Lett.* 65, 3019–3021 (1994).
41. Kovtyukhova, N. I. et al. Layer-by-layer assembly of rectifying junctions in and on metal nanowires. *J. Phys. Chem. B* 105, 8762–8769 (2001).
42. Laser -Wikipedia. Available at: <https://en.wikipedia.org/wiki/Laser>.
43. Khaled Habiba¹, Vladimir I. Makarov¹, Brad R. Weiner² & Gerardo Morell¹. Fabrication of Nanomaterials by Pulsed Laser Synthesis (PDF Download Available). *Manuf. Nanostructures* 263–292 (2014). doi:10.13140/RG.2.2.16446.28483
44. Bäuerle, D. in *Laser Processing and Chemistry* 53, 13–38 (2011).

45. Hamad, A. H. in High energy and short pulse lasers (ed. Viskup, R.) 306–325 (InTech, 2016). doi:10.5772/61628
46. Momma, C. et al. Short-pulse laser ablation of solid targets. *Opt. Commun.* 129, 134–142 (1996).
47. Brown, M. S. & Arnold, C. B. Fundamentals of Laser-Material Interaction and Application to Multiscale Surface Modification. *Laser Precis. Microfabr.* 91–120 (2010). doi:10.1007/978-3-642-10523-4
48. Lucas, L. & Zhang, J. Femtosecond laser micromachining: A back-to-basics primer. *Industrial Laser Solutions* 1–22 (2012).
49. Isik, T., Kundu, S., Gunduz, I. E. & Ortalan, V. Investigation of Nanoparticle Reactions with Laser Heating by In situ TEM. *Microsc. Microanal.* 23 (Suppl, 1892–1893 (2017).
50. Rischel, C. et al. Femtosecond time-resolved X-ray diffraction from laser-heated organic films. *Nature* 390, 490–492 (1997).
51. Raksi, F. et al. Ultrafast x-ray absorption probing of a chemical reaction. *J. Chem. Phys.* 104, 6066–6069 (1996).
52. Ortalan, V. & Zewail, A. H. 4D scanning transmission ultrafast electron microscopy: Single-particle imaging and spectroscopy. *J. Am. Chem. Soc.* 133, 10732–10735 (2011).
53. Kwon, O.-H., Barwick, B., Park, H. S., Baskin, J. S. & Zewail, A. H. 4D visualization of embryonic, structural crystallization by single-pulse microscopy. *Proc. Natl. Acad. Sci. U. S. A.* 105, 8519–8524 (2008).
54. Taheri, M. L. et al. In situ laser crystallization of amorphous silicon: Controlled nanosecond studies in the dynamic transmission electron microscope. *Appl. Phys. Lett.* 97, (2010).
55. LaGrange, T., Campbell, G. H., Turchi, P. E. A. & King, W. E. Rapid phase transformation kinetics on a nanoscale: Studies of the α - β transformation in pure, nanocrystalline Ti using the nanosecond dynamic transmission electron microscope. *Acta Mater.* 55, 5211–5224 (2007).
56. Park, H. S., Kwon, O. H., Baskin, J. S., Barwick, B. & Zewail, A. H. Direct observation of martensitic phase-transformation dynamics in iron by 4D single-pulse electron microscopy. *Nano Lett.* 9, 3954–3962 (2009).
57. Flannigan, D. J. & Zewail, A. H. 4D electron microscopy: Principles and applications. *Acc. Chem. Res.* 45, 1828–1839 (2012).

58. Barwick, B., Park, H. S., Kwon, O.-H., Baskin, J. S. & Zewail, A. H. 4D Imaging of Transient Structures and Morphologies in Ultrafast Electron Microscopy. *Science* (80-.). 322, 1227–1231 (2008).
59. Flannigan, D. J., Samartzis, P. C., Yurtsever, A. & Zewail, A. H. Nanomechanical motions of cantilevers: direct imaging in real space and time with 4D electron microscopy. *Nano Lett.* 9, 875–881 (2009).
60. Flannigan, D. J., Lobastov, V. A. & Zewail, A. H. Controlled nanoscale mechanical phenomena discovered with ultrafast electron microscopy. *Angew. Chemie - Int. Ed.* 46, 9206–9210 (2007).
61. Flannigan, D. J., Park, S. T. & Zewail, A. H. Nanofriction visualized in space and time by 4D electron microscopy. *Nano Lett.* 10, 4767–4773 (2010).
62. Energetic material. Available at: https://en.wikipedia.org/wiki/Energetic_material.
63. Zarko, V. E. & Gromov, A. A. Energetic Nanomaterials: Synthesis, Characterization, and Application. *Energetic Nanomaterials: Synthesis, Characterization, and Application* (2016). doi:10.1016/C2014-0-01661-9
64. HMX. Available at: <https://en.wikipedia.org/wiki/HMX>.
65. Brill, T. B. & Karpowicz, R. J. Solid phase transition kinetics: the role of intermolecular forces in the condensed-phase decomposition of HMX. *J. Phys. Chem.* 86, 4260–4265 (1982).
66. Soni, P., Sarkar, C., Tewari, R. & Sharma, T. D. HMX polymorphs: Gamma to beta phase transformation. *J. Energ. Mater.* 29, 261–279 (2011).
67. RDX. Available at: <https://en.wikipedia.org/wiki/RDX>.
68. Davidson, A. J. et al. Explosives under pressure—the crystal structure of γ -RDX as determined by high-pressure X-ray and neutron diffraction. *CrystEngComm* 10, 162–165 (2008).
69. Karpowicz, R. J. & Brill, T. B. Comparison of the molecular structure of hexahydro-1,3,5-trinitro-s-triazine in the vapor, solution, and solid phases. *Journal of Physical Chemistry* 88, 348–352 (1984).
70. Goto, N. et al. Crystal structure of the high-pressure phase of hexahydro-1,3,5-trinitro-1,3,5-triazine (γ -RDX). *J. Phys. Chem. B* 110, 23655–9 (2006).
71. Millar, D. I. A. et al. Pressure-cooking of explosives—the crystal structure of ϵ -RDX as determined by X-ray and neutron diffraction. *Chem. Commun.* 46, 5662–5664 (2010).

72. Rennie, A. J. R., Martins, V. L., Smith, R. M. & Hall, P. J. Influence of Particle Size Distribution on the Performance of Ionic Liquid-based Electrochemical Double Layer Capacitors. *Sci. Rep.* 6, 22062 (2016).
73. Zhurov, V. V., Zhurova, E. A., Stash, A. I. & Pinkerton, A. A. Importance of the consideration of anharmonic motion in charge-density studies: A comparison of variable-temperature studies on two explosives, RDX and HMX. *Acta Crystallogr. Sect. A Found. Crystallogr.* 67, 160–173 (2011).
74. Millar, D. I. A. et al. The crystal structure of β -RDX - An elusive form of an explosive revealed. *Chem. Commun.* 562–564 (2009). doi:10.1039/b817966b
75. CL-20.
76. Simpson, R. L. et al. CL-20 performance exceeds that of HMX and its sensitivity is moderate. *Propellants, Explos. Pyrotech.* 22, 249–255 (1997).
77. Millar, D. I. A. et al. Putting the squeeze on energetic materials-structural characterization of a high-pressure phase of CL-20. *CrystEngComm* 12, 2524–2527 (2010).
78. Foltz, M. F., Coon, C. L., Garcia, F. & Nichols, A. L. The thermal stability of the polymorphs of hexanitrohexaazaisowurtzitane, part II. *Propellants, Explos. Pyrotech.* 19, 133–144 (1994).
79. Russell, T. P., Miller, P. J., Piermarini, G. J. & Block, S. High-pressure phase transition in γ -hexanitrohexaazaisowurtzitane. *J. Phys. Chem.* 96, 5509–5512 (1992).
80. Zhang, J. & Zhang, L. Nanostructures for surface plasmons. *Adv. Opt. Photonics* 4, 157 (2012).
81. Plasmonic.net-- Plasmonics and Nanophotonics Studies by Koichi Okamoto. Available at: <http://www.plasmonic.net/Pages/Research.aspx>.
82. Hammond, J. L., Bhalla, N., Rafiee, S. D. & Estrela, P. Localized surface plasmon resonance as a biosensing platform for developing countries. *Biosensors* 4, 172–188 (2014).
83. Yee, K. S. Numerical Solution of Initial Boundary Value Problems Involving Maxwell's Equations in Isotropic Media. *IEEE Transactions on Antennas and Propagation* 14, 302–307 (1966).
84. Reddy, J. J. N. An Introduction to the Finite Element Method. *Essentials Finite Elem. Method* 684 (1993). doi:10.1109/MM.1986.304778
85. Yu, B. et al. A Short Course on Boundary Element Methods. *Tara* 91, 243–274 (2015).
86. Yurkin, M. A. & Hoekstra, A. G. The discrete dipole approximation: An overview and recent developments. *J. Quant. Spectrosc. Radiat. Transf.* 106, 558–589 (2007).

87. Yee cell. Available at: <https://fdtd.wikispaces.com/The+Yee+Cell>.
88. Oskooi, A. F. et al. Meep: A flexible free-software package for electromagnetic simulations by the FDTD method. *Comput. Phys. Commun.* 181, 687–702 (2010).
89. Klinger, M. & Jäger, A. Crystallographic Tool Box (CrysTBox): Automated tools for transmission electron microscopists and crystallographers. *J. Appl. Crystallogr.* 48, 2012–2018 (2015).
90. Xu, X., Isik, T., Kundu, S. & Ortalan, V. Investigation of laser-induced inter-welding between Au and Ag nanoparticles and the plasmonic properties of welded dimers. *Nanoscale*, accepted manuscript (2018).
91. Ding, S.-Y. et al. Nanostructure-based plasmon-enhanced Raman spectroscopy for surface analysis of materials. *Nat. Rev. Mater.* 1, 16021 (2016).
92. José-Yacamán, M. et al. Surface diffusion and coalescence of mobile metal nanoparticles. *J. Phys. Chem. B* 109, 9703–9711 (2005).
93. Lehtinen, K. E. J. & Zachariah, M. R. Effect of coalescence energy release on the temporal shape evolution of nanoparticles. *Phys. Rev. B* 63, 205402 (2001).
94. Pennycook, S. J. et al. Aberration-corrected scanning transmission electron microscopy: From atomic imaging and analysis to solving energy problems. *Philos. Trans. R. Soc. A Math. Phys. Eng. Sci.* 367, 3709–3733 (2009).
95. De Boer, F. R., Boom, R., Mattens, W. C. M., Miedema, A. R. & Niessen, A. K. *Cohesion in Metals. Transition Metal Alloys*, North-Holland, Amsterdam 1, (1988).
96. Skriver, H. L. & Rosengaard, N. M. Surface energy and work function of elemental metals. *Phys. Rev. B* 46, 7157 (1992).
97. Grouchko, M. et al. Merging of metal nanoparticles driven by selective wettability of silver nanostructures. *Nat. Commun.* 5, (2014).
98. Hodak, J. H., Henglein, A., Giersig, M. & Hartland, G. V. Laser-induced inter-diffusion in AuAg core–shell nanoparticles. *J. Phys. Chem. B* 104, 11708–11718 (2000).
99. Shibata, T. et al. Size-dependent spontaneous alloying of Au–Ag nanoparticles. *J. Am. Chem. Soc.* 124, 11989–11996 (2002).
100. Pedersen, D. B., Wang, S., Scott Duncan, E. J. & Liang, S. H. Adsorbate-induced diffusion of Ag and Au atoms out of the cores of Ag@Au, Au@Ag, and Ag@AgI core-shell nanoparticles. *J. Phys. Chem. C* 111, 13665–13672 (2007).

101. Romero, I., Aizpurua, J., Bryant, G. W. & García De Abajo, F. J. Plasmons in nearly touching metallic nanoparticles: singular response in the limit of touching dimers. *Opt. Express* 14, 9988 (2006).
102. Keating, C. D. & Natan, M. J. Striped metal nanowires as building blocks and optical tags. *Adv. Mater.* 15, 451–454 (2003).

VITA

XIAOHUI XU

EDUCATION

- | | |
|--|----------------------|
| Materials Engineering, Purdue University | <i>2016—2018</i> |
| ○ Master of Science Overall GPA: 4.00/4.00 | <i>Indiana, USA</i> |
| Mechanical and Aerospace Engineering, Tohoku University | <i>2015—2016</i> |
| ○ Exchange student, Junior Year Program in English (“JYPE”) | <i>Sendai, Japan</i> |
| Material Science and Engineering, Xiamen University | <i>2012—2015</i> |
| ○ Bachelor of Engineering Overall GPA: 3.83/4.00 (1/99) | <i>Xiamen, China</i> |

RESEARCH EXPERIENCE

In situ investigation of laser-matter interaction using ultrafast TEM

- Investigated the interaction of pulsed laser with energetic materials.

Designation and exploration of metallic nanostructures with novel plasmonic properties

- Study of the structural and compositional evolution of noble metallic nanowires/nanoparticles under laser irradiation using (S)TEM, EDS, SEM, etc.
- Studied the optical properties of laser-welded Ag-Au nanostructures using ultrafast TEM and simulation methods including FDTD and DDA.

Research on advanced electron microscopy technique—ultrafast TEM

- Systematically learned the operation of ultrafast TEM to achieve both high temporal (picosecond, femtosecond) and spatial (nanometer) resolution.
- Learned the principles and alignment of ultrafast lasers.

PUBLICATIONS

- X. Xu**, T. Isik *et al*, *in situ* investigation of laser-induced inter-welding of Au-Ag NPs and plasmonic properties of welded Ag-Au dimers, *Nanoscale*, 2018, accepted.
- X. Xu**, S. Kundu *et al*, Investigation of Laser-induced Welding Between Gold and Silver Nanostructures by Advanced TEM Techniques, *Microsc. Microanal.* 24 (Suppl 1), 2018. doi: 10.1017/S1431927618008796.
- S. Kundu, **X. Xu** *et al*, Direct visualization of Ag nanojunction and nanogap formation by ultrafast TEM with pulsed laser heating, paper under preparation.
- S. Kundu, **X. Xu** *et al*, Direct visualization of laser-induced merging and alloying of Au into Ag nanowires, paper under preparation.
- T. Isik, **X. Xu** *et al*, Investigation of Polymer Matrix Nano-Aluminum Composites with Pulsed Laser Heating by Ultrafast TEM, *Journal of Applied Physics*, under review.
- X. Xu**, Y. Mao *et al*, Effects of oxidation cross-linking and sintering additives (TiN, B) on the formation and heat-resistant performance of polymer-derived SiC (Ti, B) films, *Ceramics International* 42 (7), 8636-8644.
- L. Liao, Z. Chen, **X. Xu** *et al*, Effects of oxidation curing and sintering temperature on the microstructure formation and heat transfer performance of freestanding polymer-derived SiC films for high-power LEDs, *Ceramics International* 44 (6), 6072-6080.